Development of a Diffused Junction Silicon Solar Cell Pilot Line

by

Guy Pickett

A Thesis Presented in Partial Fulfillment
of the Requirements for the Degree
Master of Science

Approved April 2014 by the
Graduate Supervisory Committee:

Stuart Bowden, Chair
Christiana Honsberg
Mariana Bertoni

ARIZONA STATE UNIVERSITY

May 2014

ABSTRACT

In the interest of expediting future pilot line start-ups for solar cell research, the development of Arizona State University's student-led pilot line at the Solar Power Laboratory is discussed extensively within this work. Several experiments and characterization techniques used to formulate and optimize a series of processes for fabricating diffused-junction, screen-printed silicon solar cells are expounded upon. An experiment is conducted in which the thickness of a PECVD deposited anti-reflection coating (ARC) is varied across several samples and modeled as a function of deposition time. Using this statistical model in tandem with reflectance measurements for each sample, the ARC thickness is optimized to increase light trapping in the solar cells. A response surface model (RSM) experiment is conducted in which 3 process parameters are varied on the PECVD tool for the deposition of the ARCs on several samples. A contactless photoconductance decay (PCD) tool is used to measure the dark saturation currents of these samples. A statistical analysis is performed using JMP in which optimum deposition parameters are found. A separate experiment shows an increase in the passivation quality of the a-SiN_x:H ARCs deposited on the solar cells made on the line using these optimum parameters.

A RSM experiment is used to optimize the printing process for a particular silver paste in a similar fashion, the results of which are confirmed by analyzing the series resistance of subsequent cells fabricated on the line. An in-depth explanation of a more advanced analysis using JMP and PCD measurements on the passivation quality of 3 aluminum back-surface fields (BSF) is given. From this experiment, a comparison of the means is conducted in order to choose the most effective BSF paste for cells fabricated on the line. An experiment is conducted in parallel which confirms the results via V_{oc}

measurements. It is shown that in a period of 11 months, the pilot line went from producing a top cell efficiency of 11.5% to 17.6%. Many of these methods used for the development of this pilot line are equally applicable to other cell structures, and can easily be applied to other solar cell pilot lines.

ACKNOWLEDGEMENTS

I would like to thank Drs. Stuart Bowden, Christiana Honsberg, Clarence Tracy, and Stephen Goodnick for allowing me to participate in their solar power revolution, as well as for all the knowledge they have afforded me over the past few years. I would like to thank Stanislau Herasimenka, Tim Reblitz and Matthias Karow for mentoring me, and easing my transition from mechanical engineering into electrical engineering. I would like to thank Bill Dauksher, Dr. Jeff Cotter, and Dr. Douglas Montgomery who taught me the value of designed experiments and the practicality of process engineering. I'm also grateful to have had the opportunity to work with current and future PV engineers working at the SPL. These include all of the high school students up through graduate students who have participated on the student-led pilot line over the past four years. They have all aided in my understanding of PV fabrication as well as allowed me to hone my ability to teach my knowledge to others.

TABLE OF CONTENTS

CHAPTER Page

CHAPTER Page

LIST OF TABLES

TABLE Page

LIST OF FIGURES

FIGURE Page

FIGURE Page

LIST OF ABBREVIATIONS

ANOVA	Analysis of variance
AR	Aspect ratio
ARC	Anti-reflection coating
ASU	Arizona State University
BSF	Back-surface field
CCD	Central Composite Design or Charge Coupled Device, depending on context
CP	Collection probability, fraction between 0 and 1
CZ	Czochralski (method for growing crystal ingot)
DC	Direct Current
ECV	Electrochemical capacitance voltage
EL	Electroluminescence
HF	Hydrofluoric acid
I	Current
IPA	Isopropyl alcohol
IR	Infrared
IV	Current Voltage
J	Current density
JMP	A statistical analysis software
KOH	Potassium hydroxide

LCOE	Levelized Cost of Electricity
N	Density with units #/cm^{-3}
n	Refractive index or carrier concentration, depending on context
NREL	National Renewable Energy Lab
OED	Oxidation enhanced diffusion
P	Pressure
P5000	A PECVD tool made by Applied Materials
PCD	Photoconductance Decay
PECVD	Plasma-enhanced chemical vapor deposition
PERL	Passivated emitter and rear localized diffused BSF
PSG	Phosphosilicate glass
PV	Photovoltaic
q	Elementary charge=1.602E-19 C
QE	Quantum Efficiency
QSS	Quasi-steady state
R	Reflectance, between 0 and 1, or resistance, depending on context
R&D	Research and development
R^2	Coefficient of determination
RF	Radio frequency
RSM	Response surface modle
SEM	Scanning electron microscope
SIMS	Secondary ion mass spectrometry
SO	Snap-off distance
SPL	Solar Power Lab
SRH	Shockley-Read-Hall (defect driven recombination)

SS	Squeegee speed
t	Thickness of the region
VASE	Variable Angle Spectroscopic Ellipsometry
W	Width of the device
α	Absorption coefficient
λ	Photon wavelength in nm

1. INTRODUCTION

1.1 Background of Silicon Solar Cells

Silicon solar cell devices were introduced into the market in the 1950's with applications in space and in terrestrial communications systems by Bell Labs [1]. With a growing awareness of the adverse effects that our traditional means of harnessing energy were having on our environment, the development and implementation of solar cells progressed. They are a cleaner alternative for terrestrial power generation when compared to non-renewable fossil fuels. A simple method to quantify the "cleanliness" of photovoltaic (PV) power generation as compared to other energy sources is through their carbon footprint or greenhouse gas emissions. Figure 1 depicts a comparison of the greenhouse gas emissions of modern terrestrial power generation sources. This plot takes into account not only the emissions during electricity production, but also those emissions which result during the fabrication of the devices. In the case of PV, this takes into account the refinement of silicon and the use of energy during module fabrication. This broad definition of greenhouse gas emissions is also accountable for the large uncertainty in all cases except gas and coal, where the majority of emissions from these technologies is due to combustion of fuel [2].

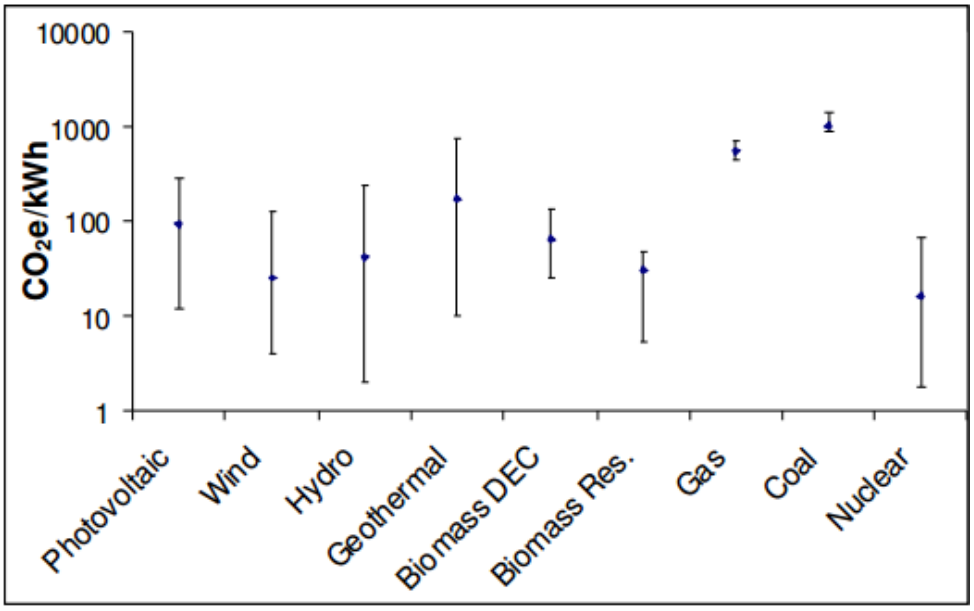

Figure 1: Comparison of Greenhouse Gas Emissions from Various Power Generation Technologies [2]

As of the year 2011, silicon based photovoltaic devices comprise 87% of world photovoltaic cell market sales [3]. One might wonder why such a large segment of the photovoltaic market rests with so few technologies, all based on one material. The answer is that the cost of the material at present is the limiting factor for the levelized cost of electricity (LCOE) of most current PV technologies on the market. Silicon is the second most abundant element on Earth, and it makes up 27.7% of the Earth's crust [4]. With consistently increasing demand for computers over the past century, which utilize silicon-based devices, silicon processing is also a more mature practice than for other more complex materials. As is shown in Figure 2, the cost of a silicon based PV modules is greatly dependent on the cost of acquiring and refining the silicon substrate itself. The trend also shows that this portion of the all-in module cost is decreasing, which is somewhat attributable to the more mature processing capabilities associated with silicon

based technologies. Thus silicon is a prime candidate for the bulk material of a solar cell device structure in today's market.

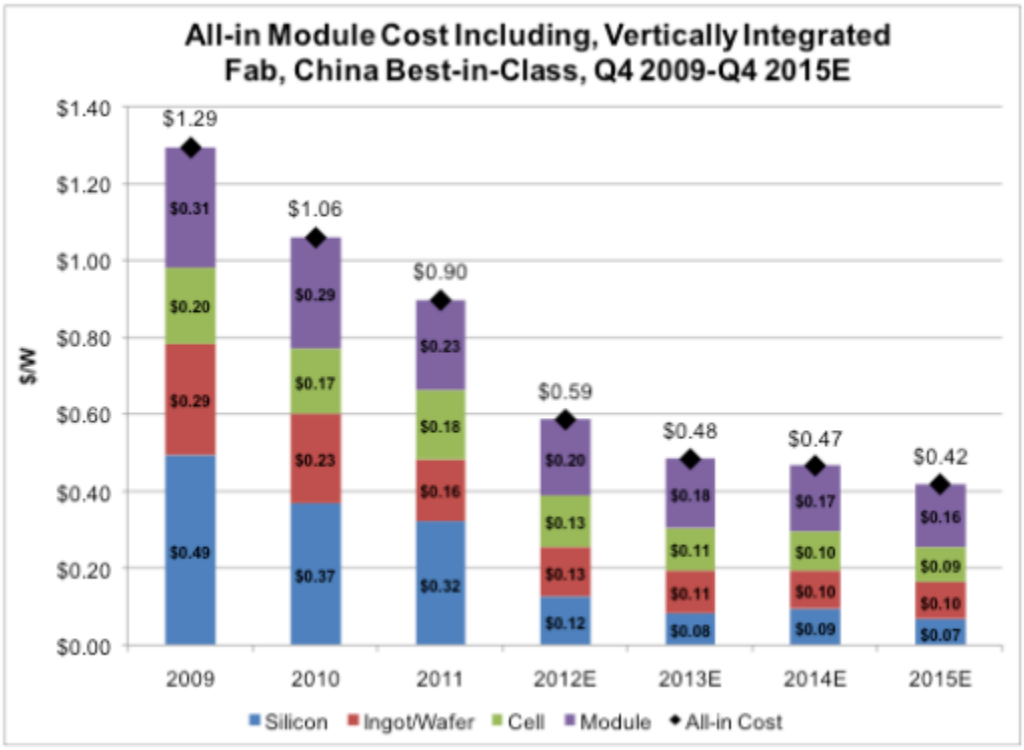

Figure 2: Breakdown and Trend of the Cost of Silicon Solar Cell Modules [5]

For the continued growth of this industry it is important that the manufacturing processes of these devices be efficient, cost effective, competitive with other sources of energy and adaptive to the ever-evolving energy market. To achieve this adaptability without significantly hindering the mass production of solar cells, it is prudent for the manufacturer to have a pilot line. This pilot line concept is usually implanted in one of two ways.

One method in a multiple-line factory is to rotate each line through a period of upgrade and process development for future technologies. This is done by temporarily halting the throughput of one line in order to exchange certain tools on the line or to add new ones to an existing flow. This method is more common in factories in that it allows for the continuous production of cells while simultaneously allowing for the implementation and development of cutting edge tools and processes for use in the factory's future product lines.

Another method is to have a dedicated pilot line for process development. This type of pilot line is more common in a pure R&D setting. This line consists of processing equipment which are capable of producing full or partial devices which can then be analyzed for quality, performance and other characteristics as needed. The equipment need not be the same tools implemented on a mass production line, and are generally more useful if their processing parameters are easily changed. These characteristics serve to make running this type of pilot line less expensive, less energy intensive, and favorable for running experiments. It is on this line in which existing processes can be analyzed and experiments for further improvement can be run. A pilot line is also an effective means to develop an initial process before committing large portions of capital to mass manufacturing equipment.

1.2 The Student-led Pilot Line at Arizona State University's Solar Power Lab

The majority of the information presented in this thesis is the result of research completed on the student-led pilot line run in the Solar Power Laboratory (SPL) located at Arizona State University's Research Park in Tempe, AZ. The first endeavor of the student-led pilot line was the formulation of a full flow diffused junction silicon solar cell

fabrication process to achieve results on par with current industry standards. This goal has since blossomed to included heterojunction thin-film silicon solar cells and n-type base solar cells. However, this thesis will focus only on the development of the diffused junction p-type base solar cell pilot line.

The Solar Power Laboratory contains all of the tools necessary to fabricate modern diffused junction solar cells and many of the tools necessary to characterize them. The specific tools used will be described as they are encountered in subsequent sections. However, the overall fabrication process is generalized to the following sequence, not to include refinement of the silicon and slicing of the substrates from silicon ingots:

1) Acquire solar grade wafers from a vendor.
2) Remove micro-cracks and texture surfaces in potassium hydroxide solution.
3) Clean wafers of metal contamination using a hydrochloric acid solution.
4) Diffuse phosphorus into the wafer to form the emitter region of the cell.
5) Etch off the phosphosilicate glass created during diffusion in a hydrofluoric acid solution.
6) Deposit a silicon nitride anti-reflection coating onto the emitter surface of the cell.
7) Print and dry the aluminum back surface field.
8) Print and dry the silver back soldering pads.
9) Print and dry the silver front contact grid onto the anti-reflection coating.
10) Fire in a belt furnace to form contacts between the metals and the silicon substrate.
11) Isolate the front-side emitter from the back-surface field using a laser edge isolation tool.
12) Characterize each cell as necessary.

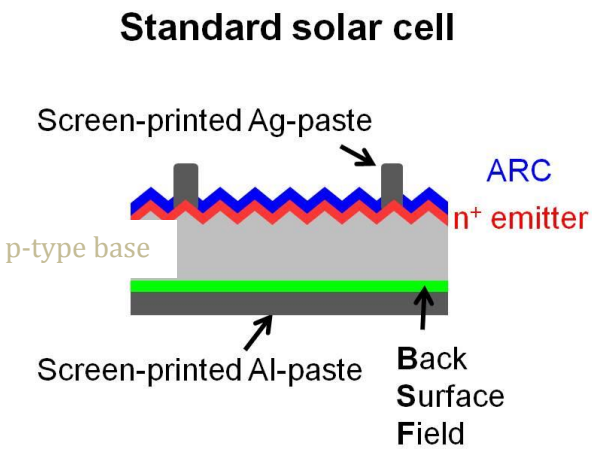

Figure 3: Cross Section Representation of a Standard Diffused Junction Si Solar Cell [6]

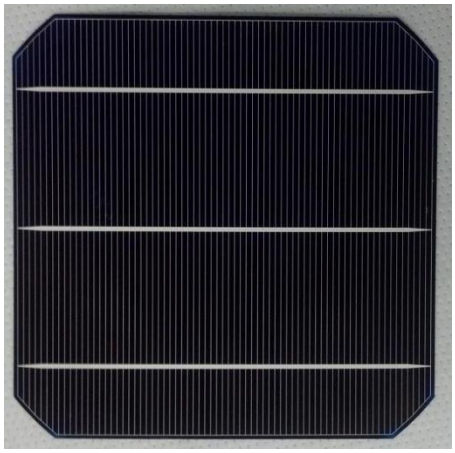

Figure 4: Top View of a Solar Cell Produced at the SPL

What is produced with this process flow is depicted in figures 3 & 4. The specific methods employed in each step, and even the number of steps for a full flow fabrication line varies between manufacturers. For instance, due to the lack of a laser for edge isolation at the SPL, a sacrificial oxide is deposited on the back of the substrate by

plasma enhanced chemical vapor deposition (PECVD) before it undergoes the emitter diffusion process. This prevents the emitter from forming on the sides and back side of the cell, thus isolating the front contact from the back. However, this practice would not be economical in a high volume process.

Many aspects of the student-led pilot line at ASU are not ideal for high-throughput processes. If this pilot line were run continuously in its present form, the estimated throughput would be about 8 wafers per hour. This varies significantly from a typical high throughput process. For instance, Spire Solar offers a turn-key solar cell fabrication line, which can produce 2,400 cells per hour [7]. However, in order to maximize profits in a semiconductor fabrication setting, it is rarely good practice to interrupt the manufacturing process to run optimization experiments or to test new processes. This is where the versatility of the pilot line comes in handy.

It is the objective of this thesis to lend insight into the specific tasks associated with the development of a diffused junction silicon solar cell pilot line. The topics discussed are not exclusive of other photovoltaic devices, and so these principles can be extended to other device structure pilot lines. This will aid in the future development of solar cell pilot lines, and ultimately to the combined effort to bring solar power to grid parity.

2. LIGHT MANAGEMENT

2.1 How light effects a solar cell

Just as is the nature of the spectrum of light emitted from our Sun complex, so are the tasks associated with designing a solar cell that can collect as much of that light as possible. Most people have an understanding that solar cells convert light into electricity, but understanding how this occurs is key to developing and optimizing a solar cell fabrication line. The basic physics principles that explain converting light into electricity will be covered here in brief. Planck's law relates the wavelength or frequency of a photon to its energy as:

$$E_{ph} = h\nu = \frac{hc}{\lambda} \qquad 2.1.1$$

In equation 2.1.1, h is Planck's constant, ν is the frequency of the photon, λ is the wavelength of the photon, and c is the speed of light. Photons with energy greater than the energy bandgap of the semiconductor can be absorbed. Silicon has an energy bandgap of 1.12 eV. This corresponds to a wavelength of approximately 1100nm. From this simple relationship, it is expected that a silicon solar cell will convert any portion of the solar spectrum with energies greater than 1.12eV into electricity. For many reasons that will be discussed in this section, this is rarely the case.

In a standard diffused junction silicon solar cell, there are three primary structural components which account for the majority of the solar cells ability to manage light collection:

1) Anti-reflection coating (ARC)
2) Textured surface(s)
3) Rear-side reflector

These will be discussed in detail along with experimental optimization procedures in later sections of this chapter. The main measurable characteristic of a solar cell that describes best its ability to collect light is its short-circuit current (I_{sc}) or short-circuit current density (J_{sc}). J_{sc} is merely the I_{sc} divided by the area of the solar cell. In an ideal situation, the J_{sc} can be described as the sum of those incoming photons, which are absorbed by the semiconductor substrate, and generate a carrier which is subsequently collected in the circuit. This is shown mathematically in the following equations:

$$J_{sc} = q\int_0^\infty QE(\lambda)N_{ph,F}(\lambda)d\lambda \qquad 2.1.2$$

$$QE(\lambda) = \int_0^W \big(1 - R(\lambda)\big)CP(\lambda, x)e^{-\alpha(\lambda)x}dx \qquad 2.1.3$$

In equations 2.1.2 and 2.1.3, q is the elementary charge, W is the width of the device, α is the absorption coefficient, x is the depth into the cell, and as before, λ represents the wavelength of the incoming photon. $N_{ph,F}$ is the number of photons of wavelength λ entering through the front surface of the cell per unit area and has units $\#\cdot cm^{-2}\cdot s^{-1}\cdot nm^{-1}$. QE(λ) is the quantum efficiency of the cell and is a fraction between 0 and 1. As the reader can see, the rate at which photons of a certain wavelength are absorbed decreases exponentially with depth,

the rate of which is described by the wavelength dependent absorption coefficient. $R(\lambda)$ is the fraction of light that is reflected at the surface of the cell, also between 0 and 1. $CP(\lambda)$ is the collection probability. This last term is a "catch-all" which encompasses recombination, transmission and parasitic absorption in the front contacts, ARC, and rear contact(s).

In practice, J_{sc}, $QE(\lambda)$, and $R(\lambda)$ are measurable and can be useful in determining where current is lost in the solar cell. Their usefulness will be described as they are used in the experimental analyses in subsequent sections. As will be shown in the next two sections, J_{sc} can be increased by introducing a textured surface as well as depositing an ARC on the front surface of the solar cell.

2.2.1 Anti-reflection Coating (ARC)

The ARC is typically a silicon nitride film deposited by plasma enhanced chemical vapor deposition (PECVD). This SiN_x ARC often has a refractive index of n=2.05 and is generally grown to a thickness of approximately 75-80nm. These properties depend on the settings of the PECVD process. For instance, the refractive index is dependent on the ratio of silane to ammonia gas flow rates during deposition and can range from 1.9 to 2.4 [8]. As might be expected, the thickness is dependent upon the deposition time. The optimum value of the refractive index and thickness of the film for this single layer ARC is quite simple to choose when considering the basic physics of optics. For a chosen wavelength, reflection can be reduced to zero by choosing the thickness of the ARC to be one quarter that wavelength divided by the films refractive index. The quarter

wavelength relationship to the thickness of the nitride described earlier is presented here as equation 2.2:

$$t_{ARC} = \frac{\lambda_{ph}}{4n_{ARC}} \qquad 2.2.1$$

This causes the reflection of light from the ARC/silicon substrate interface to destructively interfere with the reflection of light at the air/ARC interface, as they will be π radians out of phase from each other. This situation is depicted in Figure 5:

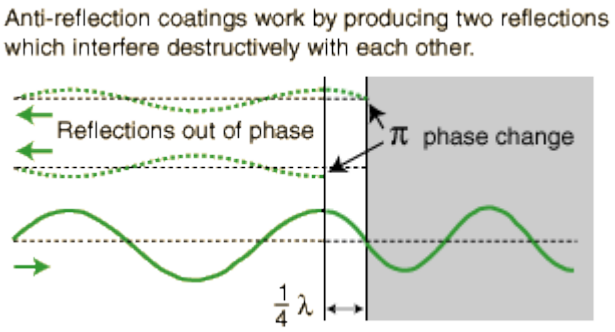

Figure 5: Schematic of Destructive Interference by an ARC [9]

Below is a plot of the intensity of the solar spectrum incident on the Earth's surface, known as the AM1.5G spectrum:

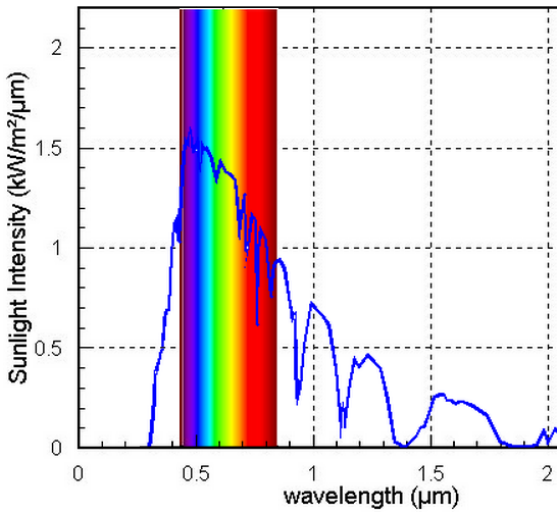

Figure 6: AM1.5G Solar Spectrum [10]

In Figure 6, the visible spectrum is highlighted by the various colors as we know them. Other than serving as an anti-reflection coating, the SiN_x also serves as a passivating layer for the front surface of the solar cell. As was mentioned previously, the index of refraction of the SiN_x is highly dependent on the ratio of silane to ammonia gas flow during deposition. This dependence is also true of the quality of the passivation for the film [8]. Therefore, an optimized film must both capture the majority of incoming radiation as well as passivate the surface satisfactorily.

Using equation 2.2, the thickness of the ARC is chosen in order to reduce, in as much as is possible, the reflection of incoming radiation from the Sun. However, optimizing for one wavelength does not necessarily optimize for the entire spectrum. In addition, most of the shorter wavelength, higher energy photons in the spectrum are absorbed by the glass encapsulate in modern solar modules.

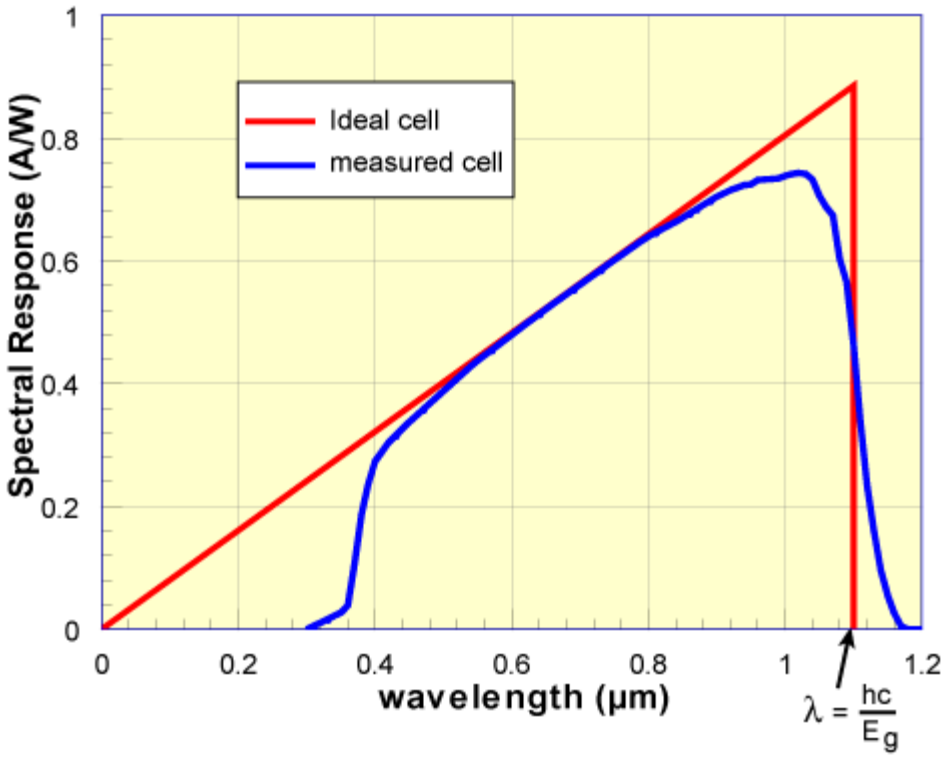

Figure 7: Measured Spectral Response of a Solar Cell Under Glass [11]

Figure 7 shows this effect where the response of the solar cell below about 400nm is truncated. These observations should all be taken into account when optimizing the thickness and refractive index of the ARC layer. One of the measurements used for this optimization is the reflectance as a function of wavelength from the solar cell measured by a reflectometer.

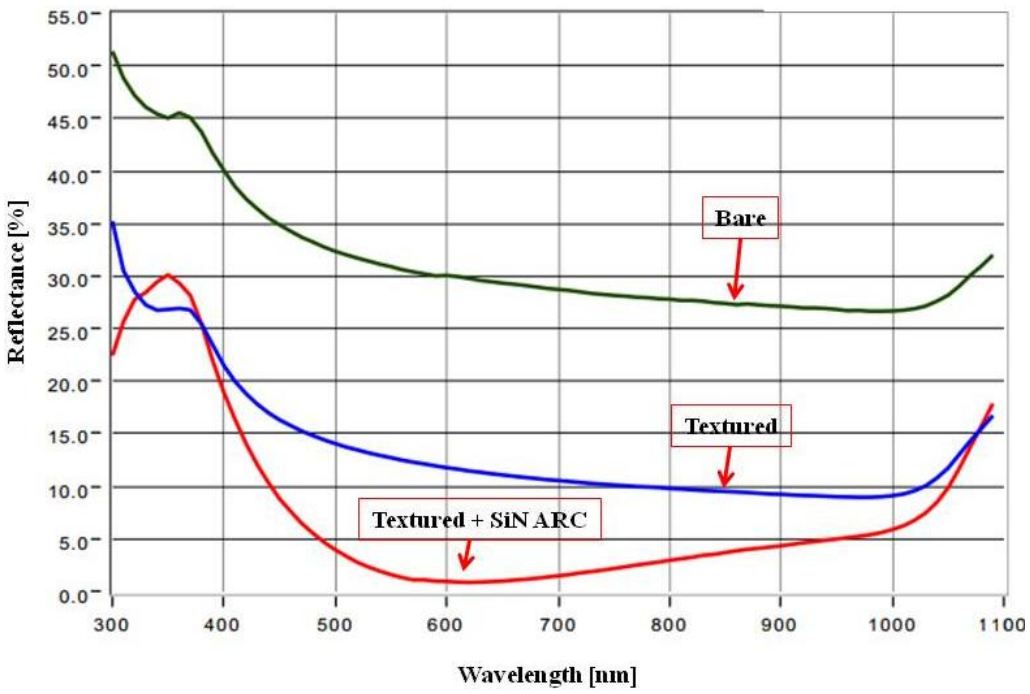

Figure 8: Reflectance Curves for Planar, Textured, SiN ARC

Figure 8 shows such a reflectance measurement for a planar as cut silicon wafer, a textured silicon wafer (texturing will be covered in the next section), and textured silicon wafer with a 78nm thick SiN_x ARC. These measurements were produced using a QEX10 measurement tool from PVMeasurements Inc. As can be seen, texturing and adding an ARC have had the effect of shifting the curve down for most wavelengths of light of interest. Comparing Figure 6 and Figure 8, one can see that optimization of the ARC thickness must take into account both the intensity of the AM1.5G solar spectrum, and the characteristic reflectance curves for a-SiN_x:H ARC on textured silicon.

2.2.2 Optimization ARC Thickness: Setup & Procedure

Initially, the thickness of the ARC was chosen such that there was a minimum reflectance at 630nm wavelength light, based on the experience of the advising faculty, who have worked extensively in the silicon solar cell industry. From equation 2.2.1, with an initial refractive index of n=2.05, this required an ARC thickness of ~77nm. As is discussed in section 4.2, the passivation quality of the front surface by the ARC is highly dependent on the gas flow ratio during PECVD deposition, but so is the refractive index. Therefore, optimization of the ARC, as stated previously, is an iterative process. Considering the practical limitations of the PECVD tool, such as control of deposition rate and passivation quality and/or refractive index, the target thickness became 78nm. This turned out to be very close to the optimum thickness for the cells made at the SPL, as is demonstrated in this experiment. For optimization purposes, the following experiment would be repeated after the passivation experiments described in

section 4.2, for a true optimization, and so on until a film is derived which exhibits excellent passivation quality as well as excellent light trapping capability.

In order to optimize the thickness of the ARC, a lot containing 7 samples was processed with varied ARC thicknesses. These samples were 6 inch round, 675µm thick, 1-5 Ω-cm, <100> silicon wafers with one side polished and the other side left as-cut. The ARCs were deposited on the polished sides. The reason for using these substrates rather than solar cell grade substrates is that an accurate reflectometer thickness measurement requires a polished surface. The following is a sampling of the resultant reflectance vs wavelength curves for this experiment:

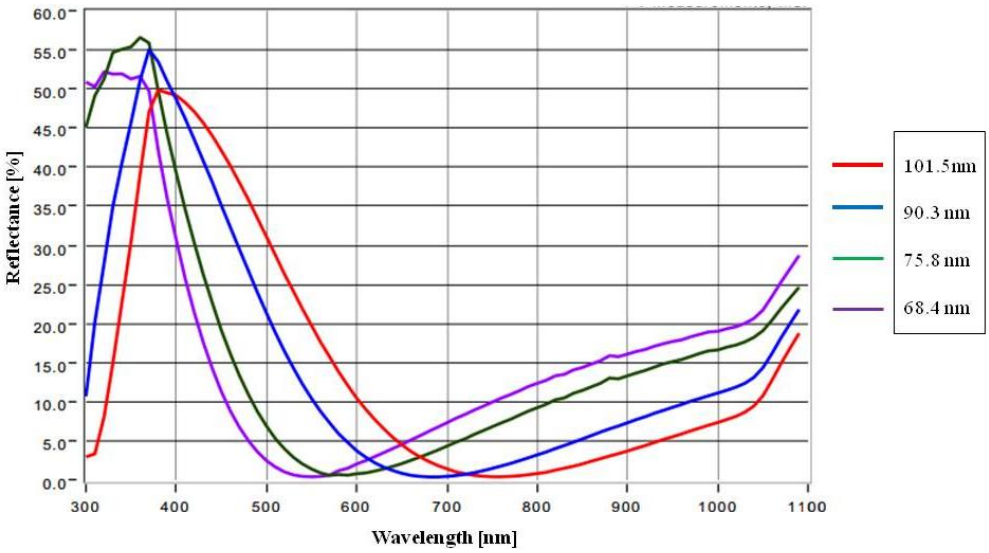

Figure 9: Effect of Varied SiN_x ARC Thickness on Reflectance

The run matrix for this experiment is depicted in Table 1:

Table 1: SiN ARC Thicknes Experimental Matrix

Sample ID	**Dep Time (s)**
1	16
2	14
3	17
4	18
5	15
6	13.5
7	13

This experiment was run using an Applied Materials P5000 PECVD tool. All parameters, except deposition time, were held constant, to include wafer temperature, pressure, gap, and RF power. At the conclusion of the sample depositions, the reflectance vs photon wavelength curves were measured using PVMeasurements QEX10 tool, and the thickness of the deposited films were measured using a reflectometer. This allows for a fit of the ARC thickness as a function of deposition time, from which the deposition time of a desired ARC thickness may be calculated, pending the results of the power density calculations.

In order to find the optimum thickness which results in the maximum amount of radiation trapping, the AM1.5G spectrum, available as an Excel sheet

on NREL's website [12], can be used in conjunction with the measured reflectance curves for each ARC thickness sample. The radiation power density captured at each wavelength is calculated as:

$$P = \int_{400nm}^{1100nm} p_{AM1.5G}(\lambda)\big(1 - R(\lambda)\big)d\lambda \qquad 2.2.2$$

Bearing in mind that most of spectrum below 400nm is absorbed by the glass in a solar module, this result is integrated between 400-1100nm for each ARC thickness to give a good approximation as to which thickness will yield the highest power density. At the conclusion of this experiment to find the optimum ARC thickness for light trapping, the experiment described in section 4.2 is then run in order to optimize passivation quality of the film. Pending the results of that experiment, should the refractive index of the film change, this experiment would then be run again.

2.2.3 Optimization ARC Thickness: Results & Discussion

The plot showing the results of the ARC thickness vs deposition time is shown in Figure 10:

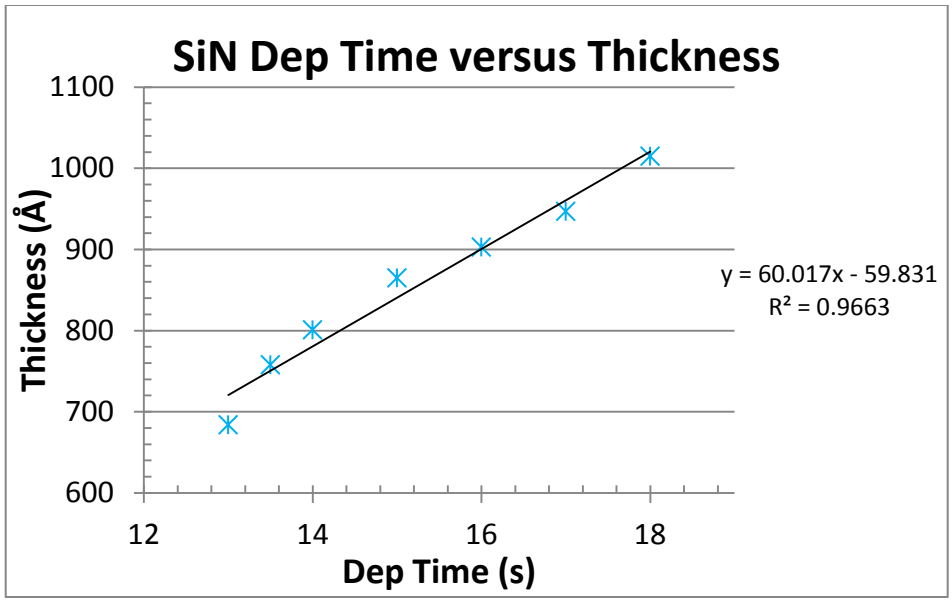

Figure 10: ARC Thickness vs Deposition Time

From this, a linear fit was calculated, the equation of which is included in Figure 10. It shows that with all other conditions being fixed at what values they are, the P5000 deposits this film at a rate of approximately 6nm/s. The power density for each ARC thickness is plotted in Figure 11:

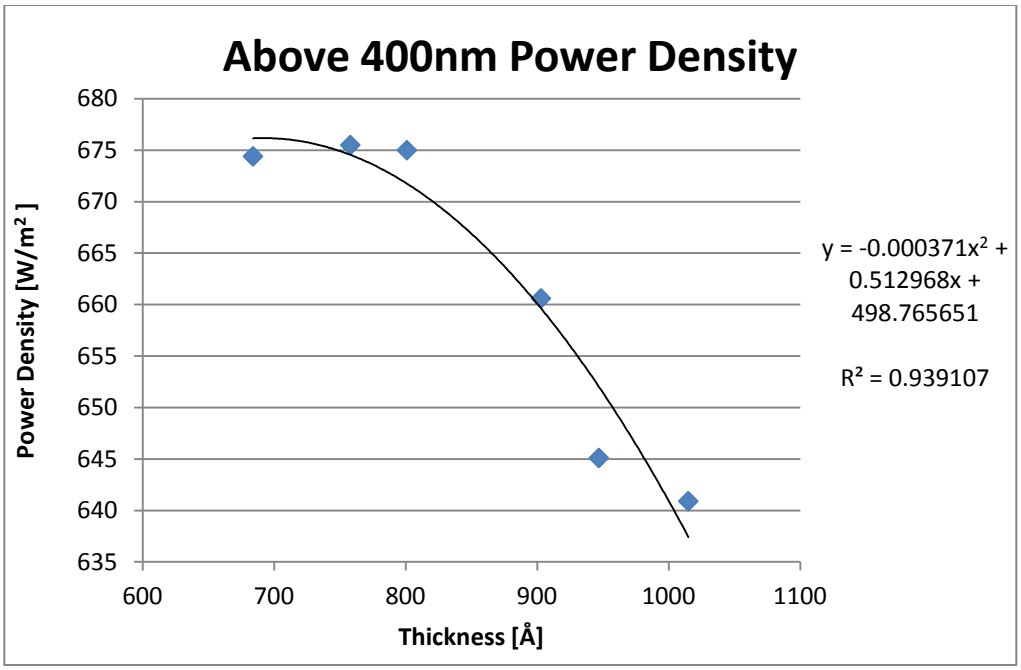

Figure 11: Power Density vs ARC Thickness

The results were fitted using a 2nd degree polynomial. From this fit, a maximum power density is estimated to occur with an ARC thickness of 70nm. This is not much less than the initial 78nm used at start-up. The reader may be concerned that optimizing for thickness on polished wafers will not yield an optimized result when transferred to textured solar cell grade wafers. To ensure that this is not the case, Figure 12 shows that there is little concern here:

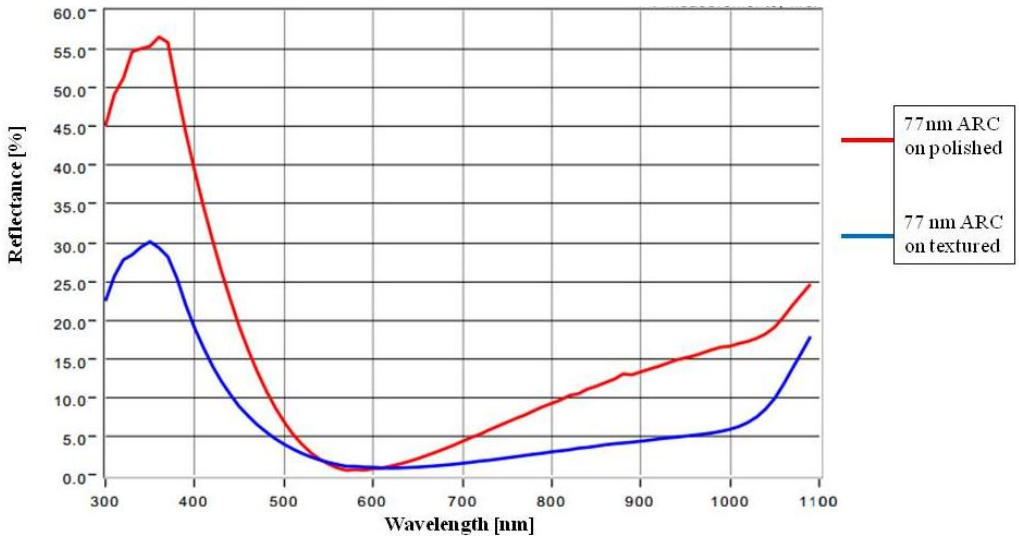

Figure 12: Effect on Reflectance of ARC on Polished vs ARC on Textured Wafer

Although there appears to be a minor shift in the minimum reflectance wavelength to the right on the textured wafer, the curve itself is relatively flat in this region. If the researcher were so inclined, now knowing the vicinity of the ARC thickness that results in the highest power density, the researcher could easily implement another optimization experiment using textured wafers. These samples would then have their reflectance curves measured and there power densities calculated against the AM1.5G spectrum using the same method as above.

I would like to thank Dr. Vivek Sharma and Bill Dauksher, who fabricated and measured these samples.

2.3 Textured Surfaces

Another processing technique used to reduce reflectance from a silicon solar cell is commonly referred to as texturing. The goal of texturing is to form pyramids on the surfaces of the substrate in order to increase the likelihood that light reflected from one surface of the substrate will be transmitted by another surface of the substrate. This scheme is depicted in Figure 13:

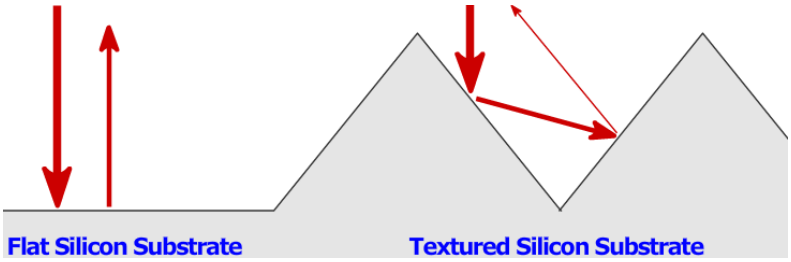

Figure 13: Schematic of Generic Reflectance Pattern for Flat and Textured Substrates [10]

The increasingly thinner arrows represent the smaller fraction of incoming light that is reflected upon each interaction with the air/substrate interface. Although there are several texturing schemes in use, the most common texturing method uses a potassium hydroxide or sodium hydroxide based solution to form random pyramids in the surface of the silicon substrates. A scanning electron microscope (SEM) image of the result is shown in:

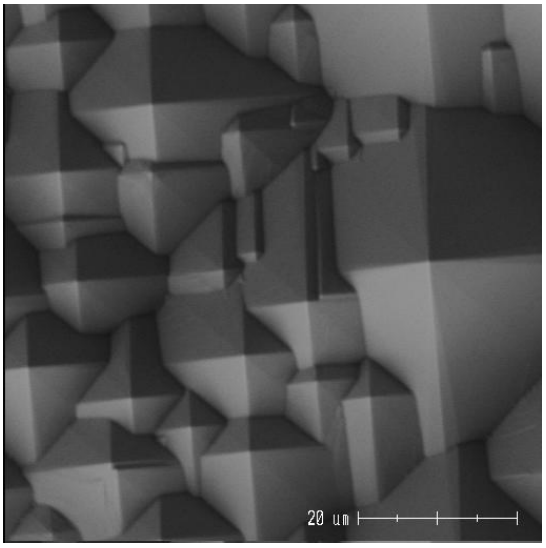

Figure 14: Top View of Si Textured in KOH Solution at SPL [13]

As of yet, there does not appear to be a complete understanding of the mechanism that takes place during texturing to form the pyramids on the surface of a silicon substrate. There are several groups that have attempted to characterize and optimize this process, but results appear to vary greatly between these groups. This large variability has also been observed at the SPL, in which there is even a large difference in the quality of texturing between users of the same equipment. The mechanisms discussed in this thesis are only relevant to <100> mono-crystalline silicon wafers, as these are the wafers used at the SPL. Most silicon solar cell manufacturers use wafers of this orientation.

Vazsonyi, et. al. have proposed an anisotropic etch mechanism to explain this random pyramid formation during a dilute alkaline etch [14]. Their experiments show that for solutions of low alkaline content, 1.5-4 wt% for NaOH, and concentrations of isopropyl alcohol (IPA) between 3-10 vol%, there is a preferential etch of the <100> plane over the <111> plane. This results in randomly distributed pyramids across the wafer surface, both in size and position, the sides of which consist of {111} crystal planes.

Several experiments were run in order to formulate various texturing recipes on the pilot line, based on the available equipment at the time. Texturing started in a 10 liter glass beaker, on a hot plate. This process was then moved into an acid hood, which contained a 20 liter heated, stainless steel bath to hold the texturing solution. Eventually, this stainless steel bath was replaced by a 10 liter quartz bath, which was found to be too small to texture cell lots in a repeatable manner. This 10L quartz bath was replaced by a 20L quartz bath. The outcome from all of these process changes served to show that texturing is inherently variable. For each new setup, an experiment was run in which five parameters were varied between three levels:

1) 1, 2, and 3 wt% KOH
2) 5, 7, and 9 v% IPA
3) Time: 50, 75, and 100 minutes
4) Temperature: 80, 84, and 88°C

Each operating point was run with two to four lots of 12 wafers each. It was found that uniform etching would only result once the solution had been exposed to a sufficient amount of silicon, the exact amount of which was never optimized on the line. It was typical to completely dissolve two wafers, weighing approximately 11.1g each in the solution prior to texturing. The only measurable outcomes for these experiments, however, are the etch rates and reflectance measurements. The etch rate was measured by weighing the samples before and after texturing. With a known area of the wafer and density of crystalline silicon, the thickness change in thickness after texturing can be accurately estimated. Typical etch rates are on the order of 0.14 to 0.35 μm/minute. The etch rate does not determine the quality of texturing, unfortunately. It can be correlated for one process, but does not necessarily translate to another. The etch rate was only

used to determine when and how much KOH to add to the solution after each batch of wafers was run through it.

For a uniformly textured sample, the reflectance would be a reasonable measure of the quality of texturing. Uniformity is, unfortunately, usually the problem when bringing up a texturing process. Any processes undergone by the samples prior to texturing could affect the uniformity. For this reason, many different schemes were formulated with the advent of new equipment, even when that equipment was not directly involved in the texturing process. Specific results will not be discussed in this work, as they will likely not be useful to the reader. As was mentioned, there are several documented attempts by other groups to characterize texturing in general, but their results are not very useful other than to bound the initial experiments, as is done in the proposed experiment above.

3. FORMING THE EMITTER

3.1 $POCl_3$ Diffusion

A common technique used in industry for forming emitters is known generally as $POCl_3$ diffusion. The main elements of this process are a furnace and a bubbler, which contains liquid $POCl_3$. A simplified schematic of this setup is shown in Figure 15:

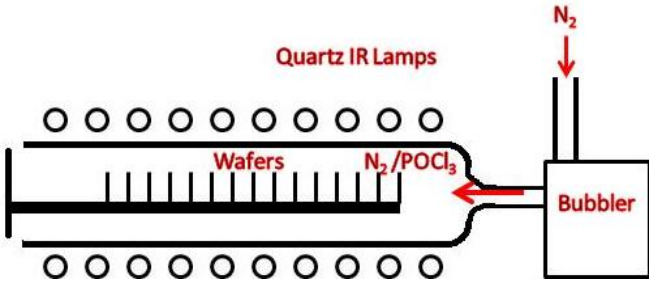

Figure 15: $POCl_3$ Diffusion Furnace General Schematic

For high throughput, the wafers are placed horizontally in quartz boats side-by-side. The boats are placed on a cantilever beam. This allows hundreds of wafers to be diffused at once in an industrial process. Quartz infrared lamps line the walls of the tube and ideally are situated in banks. This allows separate control of the heating in different sections of the tube. An inert carrier gas, such as nitrogen or argon, is flowed through the bubbler where it picks up some of the $POCl_3$ and continues to flow into the tube containing the silicon wafers. This gas amalgamation will flow across the surfaces of the wafers where the following two reactions will occur:

$$4POCl_3(g) + 3O_2(g) \rightarrow 2P_2O_5(l) + 6Cl_2(g) \quad 3.1.1$$

$$2P_2O_5(l) + 5Si(s) \rightarrow 5SiO_2(s) + 4P(s) \quad 3.1.2$$

What is left is an aggregate of P_2O_5 and SiO_2, known as phosphosilicate glass [15]. This phosphosilicate glass serves as an approximately infinite diffusion source for phosphorus. A fortunate side effect of using $POCl_3$ as a phosphorus source is that the Cl_2 gas that results from the reaction in equation 3.1.1 reacts with metal contamination on or near the surface of the substrate. This chlorine/metal gas is then vented out of the chamber. This is known as gettering. Since most metals act as recombination sites, the reduction of them in the substrate near the surface serves to decrease the surface recombination for an overall improvement in cell performance [16].

Fick's laws are often used as a first approximation of the diffusion profile of a particular dopant that will result within a specified material, but due to lack of accuracy when describing phosphorus diffusion in crystalline silicon, this method will be omitted in this work. Modeling the mechanism by which the emitter formed is also not the goal of bringing up a pilot line. The experiment presented in this section only sought to optimize an already sufficient process. In lieu of a result of Fick's laws, a phosphorus concentration vs depth profile is presented as measured by electrochemical capacitance voltage (ECV) and by secondary ion mass spectrometry (SIMS) on a cell diffused in an MRL tube furnace at the SPL:

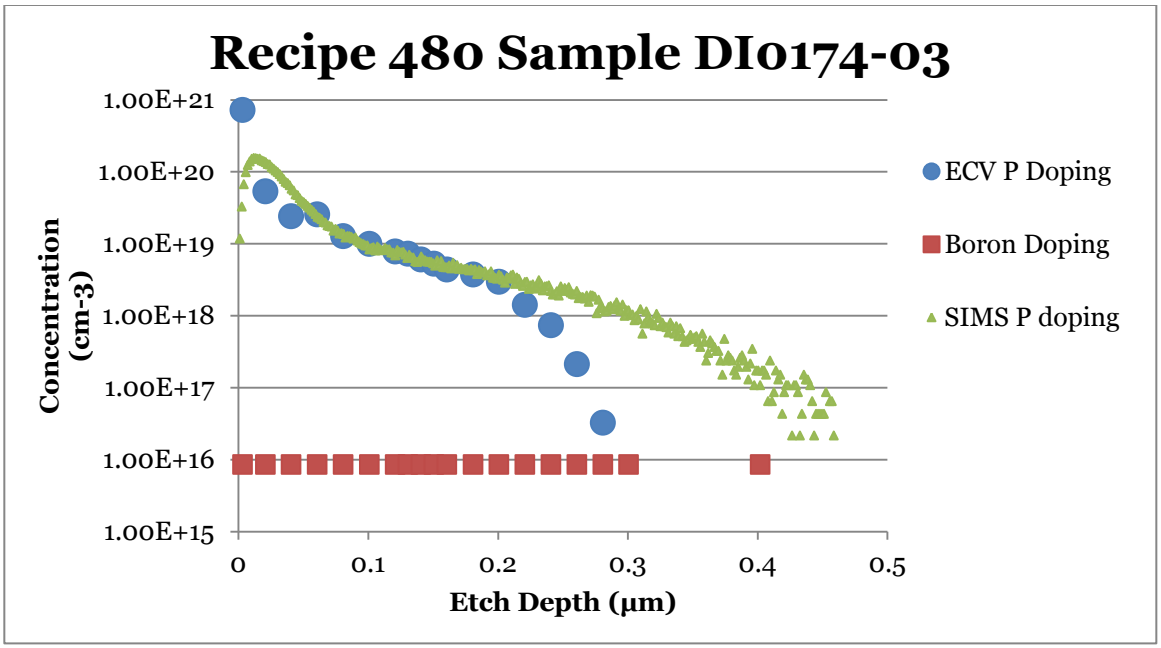

Figure 16: SIMS and ECV Profiles of Typical Emitter of SPL Cells

The key features presented in Figure 16 are the difference between SIMS and ECV measurements, and the concentration at the surface of the sample. The reason there is a difference between SIMS and ECV is that ECV is only measuring the "active" dopants in the samples, whereas SIMS measures all dopants that are knocked out of the sample by ions. For a more in depth explanation of these two measurement techniques, refer to reference [17, p. 77 & 654]. Active dopants are those dopant atoms which have substituted silicon atoms in the crystal lattice, and therefore play a role in conduction. For modeling purposes, ECV is a more useful measurement to have. ECV also yields a better profile near the surface of the sample than does SIMS. This can be observed in Figure 16 where the SIMS profile of the same sample appears to dip down near the surface. The PSG approximates an infinite source, and so this concentration near the surface is highly unlikely. The ECV profile shows that the surface concentration can be estimated by extrapolating the concentration vs depth back to the surface. Although

these are rather slow measurement techniques, their results are useful when characterizing a diffusion process.

The dopant density at the surface of the sample affects the performance of the solar cell primarily in two ways. A more heavily doped surface results in lower contact resistance between the front Ag grid and the silicon substrate [17, p. 130]. Conversely, a more heavily doped surface increases the surface recombination for minority carriers generated within the emitter, thus decreasing the V_{oc} of the cell. As was said in section 2.1, the light absorption decreases exponentially with depth into the cell. Thus, many of the possible light generated carriers to be collected are generated near the surface of the cell. With heavy doping, these generated carriers will quickly recombine. This is an optimization problem in and of itself, but again, this will not be covered in this work. Two ways in which this problem is alleviated in modern solar cells is by selectively doping the silicon more heavily only under the contacts, and by augmenting the front Ag paste such that it is able to contact more lightly doped emitters.

There are typically two primary steps in the diffusion process using $POCl_3$, and a third optional step:

1) Pre-deposition: formation of the PSG, at 800-850°C for 10-30 minutes typically.
2) Drive-in: diffusion of P from the PSG into the Si substrate, at 850-1200°C for 10-60 minutes typically.
3) Oxidation: results in oxygen-enhanced diffusion (OED) [18]. Typically done during drive-in or for some portion of the drive-in period.

This third optional step is implemented with the intent of forming an emitter with a deeper metallurgical junction, a steeper drop in dopant density with increasing depth into the wafer near the surface, and a decrease in surface dopant density. This can be

beneficial for the V_{oc} of the cell, which is dependent upon the dark saturation current I_o of the cell [19]. One contributor to I_o is surface recombination near the surface in the emitter. This recombination is exacerbated by what is known as a dead layer, which is what results when there is a very high concentration of P at the surface (on the order of 10^{20} cm^{-3}). Lighter doping within the emitter at and near the surface results in a lower recombination rate there compared to a cell with a diffusion profile in which the concentration is higher there and drops more gradually with depth into the substrate. Likewise, a decreased recombination rate results in a larger diffusion length for minority carriers generated within the emitter. Then more of these generated carriers are collected with a deeper junction, which can increase I_{sc}, as well as V_{oc} which has a weak logarithmic dependence on I_{sc}. For more information on OED, see reference [20], which describes how oxidation increases the vacancies in the lattice by a factor of up to 10x that at thermal equilibrium in silicon. It also provides an excellent description of how an increase in vacancy density increases diffusivity of phosphorus in silicon.

The effect of OED was observed between two $POCl_3$ diffusion recipes used to fabricate solar cells on the student-led pilot line at the SPL. Figure 17 shows the ECV profiles of three 1-5 Ω-cm CZ, 675μm thick, single-side polished wafers diffused using one of the two recipes.

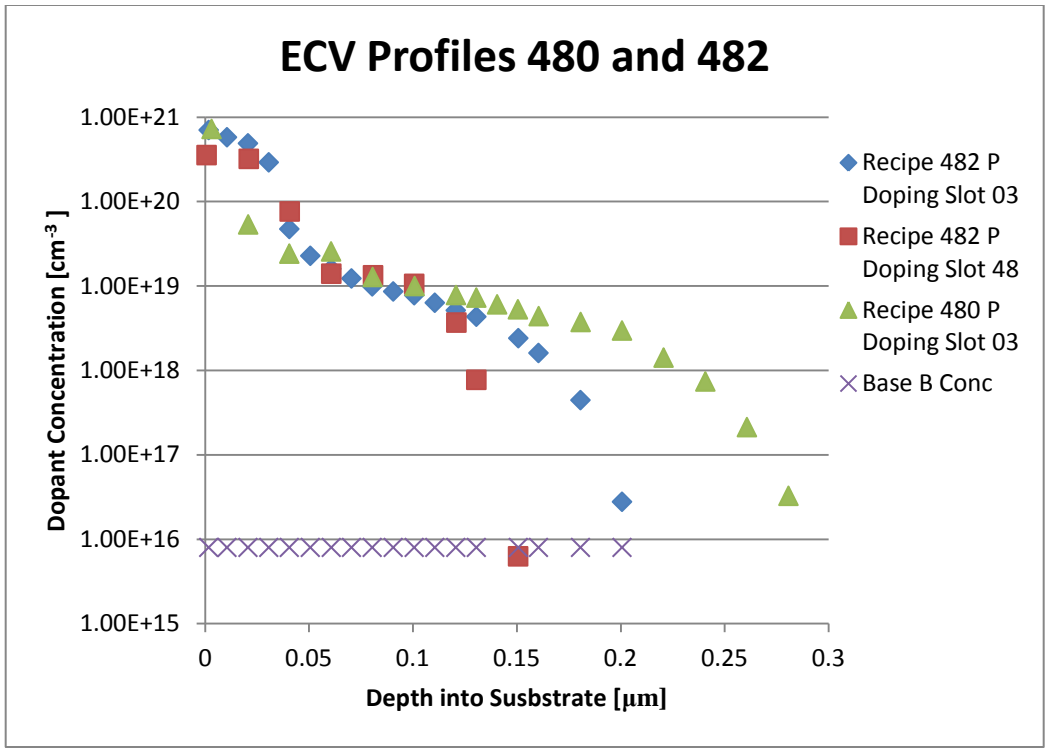

Figure 17: Comparison of Diffusion Profiles with and Without OED

Recipe 480 implements OED after an ~30 minute drive-in step at a nominal temperature of 850˚C (the actual temperature varies across the tube for uniformity). Recipe 482 does not include this oxidation step, but is diffused for similar times and temperatures.

The effects of the two different diffusion profiles on cell performance were compared for several symmetric samples. Using a photoconductance decay (PCD) method, the contribution to the dark saturation current due to the front emitter/ARC surface $J_{o,F}$ to the solar cell were measured. More information on this technique and its usefulness in circumventing undesirable noise due to other processing can be found in section 4.2. The results of the analysis are summarized in Figure 18, which is a statistical analysis performed on the data using JMP:

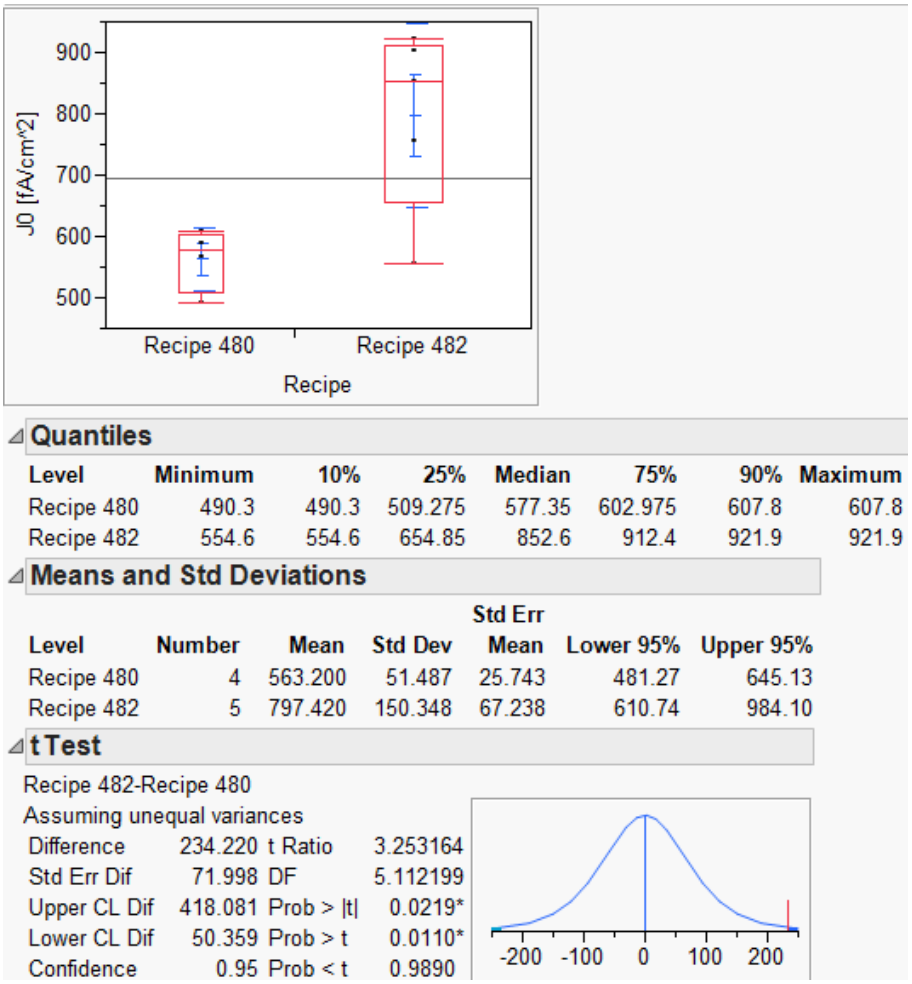

Quantiles

Level	Minimum	10%	25%	Median	75%	90%	Maximum
Recipe 480	490.3	490.3	509.275	577.35	602.975	607.8	607.8
Recipe 482	554.6	554.6	654.85	852.6	912.4	921.9	921.9

Means and Std Deviations

Level	Number	Mean	Std Dev	Std Err Mean	Lower 95%	Upper 95%
Recipe 480	4	563.200	51.487	25.743	481.27	645.13
Recipe 482	5	797.420	150.348	67.238	610.74	984.10

t Test

Recipe 482-Recipe 480
Assuming unequal variances

Difference	234.220	t Ratio	3.253164
Std Err Dif	71.998	DF	5.112199
Upper CL Dif	418.081	Prob > |t|	0.0219*
Lower CL Dif	50.359	Prob > t	0.0110*
Confidence	0.95	Prob < t	0.9890

Figure 18: JMP Analysis of $J_{o,F}$ for Two Diffusion Recipes

From Figure 18, it can be stated with 97.8% confidence that recipe 482 results in a higher dark saturation current than recipe 480. Practically, this difference of 234 fA/cm^2 translates to a difference in V_{oc} of 9mV, which is quite significant for this cell structure.

The analysis that was just presented is known as Student's t-test, and in this particular analysis, an unequal variance was assumed between the samples of the two recipes. For high throughput processes, as is often encountered in a mass manufacturing

environment, a good estimate of the variance may be made through historical data. In the case of this new recipe, recipe 482, however, few samples were created to characterize it before the previous conclusion was drawn. Therefore, rather than assuming a variance based on historical data that pertained to the more heavily used recipe 480, the calculated sample standard deviation of recipe 482 was used. This kind of simple statistical process analysis could potentially save a company a significant portion of cost associated with producing a sub-par product. Student's t-test is also covered thoroughly in Dr. Montgomery's book, should the reader be interested in learning more [21, p. 38].

I would like to thank Yan Chen of ASU and Chuqi Yi of UNSW for fabricating these samples, and Sebastian Husein of ASU for characterizing these samples by ECV.

4. SURFACE PASSIVATION

4.1 Recombination at Interfaces and Surfaces

Up until this point, not much has been said regarding recombination. Reducing recombination is typically the key to improving the performance of any minority carrier device. For a solar cell in particular, recombination is any process by which photogenerated charge carriers are lost before being collected for useful work. Without going into the details of the many different types of recombination mechanisms, the

simplest way to understand this is that the energy gained by an electron or hole is dissipated at some time before transferring its energy to the load for which it is intended. It is often the interfaces or surfaces of a device which experience the highest frequency of recombination. This is often observed for several reasons.

It is at the surfaces that foreign contamination is deposited by the external environment. It is also at surfaces and interfaces that defects within the bulk of the wafer tend to agglomerate during cell processing. More importantly, for this cell structure in particular, is that there are many "dangling" bonds at the surfaces and interfaces, meaning there are unoccupied orbitals where atoms in the crystal lattice should have a bond, but do not due to an abrupt termination of the crystal lattice at the surface or interface. Therefore, the easiest targets for reducing recombination and improving overall cell efficiency are the surfaces of the solar cell.

Due to these defects being far denser at, or very near the surface as compared to defects in the bulk of the semiconductor material, it is not useful to characterize their effect by bulk recombination or lifetime. A different parameter called $J_{o,eff}$, the dark saturation current, is measured. From this measurement, $J_{o,F}$, the component of the dark saturation current due to recombination at the emitter/ARC interface, is extracted. The most effective method for measuring this parameter is by using the photoconductance decay (PCD) method. For more information regarding this, refer to section 4.2.2 and 4.3.2.

4.2.1 Passivating the Front Surface

The clever methods that have been devised in the last six decades to passivate the front surface is a testament to the level of engineering that has gone into the modern solar cell. These methods must not only reduce recombination at the front surface, but they must also remain transparent to incoming radiation. They are also often made in such a way as to increase the light trapping capabilities of the device, such as is the case for the a-SiN_x:H anti-reflection coating (ARC) used on typical modern solar cells. The utility of the a-SiN_x:H ARC to increase light trapping of a solar cell has already been explained in section 2.2. Therefore, only its ability to passivate the front surface of a solar cell will be expounded in section 4.

To better understand how the SiN_x film serves to passivate the surface of the cell, it is prudent to consider the energy bands across the SiN_x/Si interface. This is shown in Figure 19:

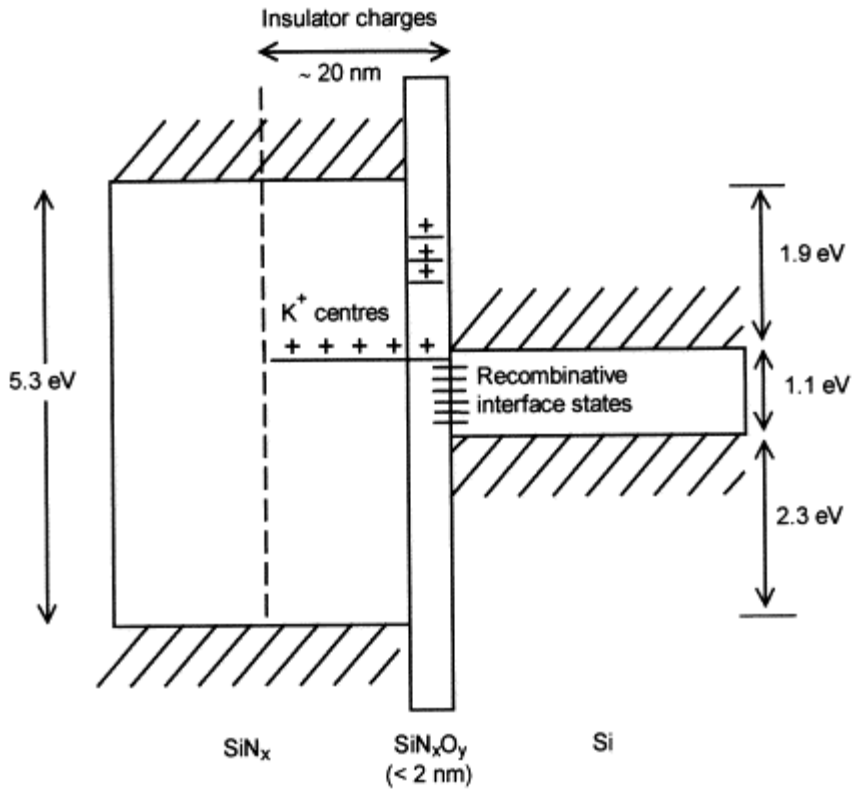

Figure 19: Energy Band Diagram SiN_x ARC/Si Interface [22]

The SiN_xO_y, or silicon oxynitride, is the result of what is initially a thin SiO_2 film grown on the silicon substrate to approximately 2nm in the PECVD chamber between the time it is loaded and the time that the SiN_x film begins to be deposited [22]. This oxide then becomes an oxynitride as the SiN_x film is grown. This results in a few interesting states beginning with dangling bonds, depicted as horizontal lines and called "Recombinative Interface States" in Figure 19. The "+" signs depicted within the thin SiN_xO_y layer represent the trapped charge within this film, that is typical of an oxide. What is then unique about this PECVD grown SiN_x film is the K^+ centers within the film due to back-bonding. Although the utility of these unique K^+ centers will not be covered

in this work, it is interesting to learn that they can be manipulated via corona charging to induce field-effect passivation of the silicon surface [23].

What is typical of these PECVD deposited a-SiN_x:H films is that the hydrogen present in the films will serve to "tie up" these dangling bonds or interface states, thus passivating the silicon surface. The ability of a PECVD deposited a-SiN_x:H film to passivate the silicon surface will change depending on several parameters during deposition. These parameters are: wafer temperature, RF power, pressure, and gas flow ratio of SiH_4:NH_3.

There are other schemes for passivating the front surface, such as field effect passivation by charged nitride films. These methods will not be covered in this work, but the characterization techniques used here are just as relevant to such advanced concepts. For more information on charged nitrides, the reader is referred to Dr. Vivek Sharma's PhD thesis, who also performed his work at the SPL on the student-led pilot line, and is a contributor to the research presented in this work [23].

4.2.2 a-SiN_x:H ARC Optimization Experiment: Setup & Procedure

This optimization experiment was performed using an Applied Materials P5000 PECVD tool at the SPL. The experimental matrix used is summarized in Table 2:

Table 2: RSM Design for SiN_x Film Optimization [23]

Sample	Pattern	Comment	Power	Pressure	Gas ratio (SiH_4 in NH_3)
			(W)	(Torr)	(sccm)
1	-00	Axial	49	3.0	49.95
2	0+0	Axial	175	4.7	49.95
3	000	Center-Ax	175	3.0	49.95
4	-++	FF	100	4.0	78.3
5	+--	FF	250	2.0	21.6
6	--+	FF	100	2.0	78.3
7	000	Center-Ax	175	3.0	49.95
8	++-	FF	250	4.0	21.6
9	-+-	FF	100	4.0	21.6
10	+-+	FF	250	2.0	78.3
11	000	Center-Ax	175	3.0	49.95
12	---	FF	100	2.0	21.6
13	00-	Axial	175	3.0	2.27
14	00+	Axial	175	3.0	97.6
15	+00	Axial	301	3.0	49.95
16	000	Center-Ax	175	3.0	49.95
17	0-0	Axial	175	1.3	49.95
18	000	Center-Ax	175	3.0	49.95
19	+++	FF	250	4.0	78.3
20	000	Center-Ax	175	3.0	49.95

RSM stands for response surface model, and is a popular designed experiments technique for determining an optimum response operating point. This particular RSM is known as a central composite design and has 6 center points with no replication of the other operating points. RSM designs are typically used when a good deal of information is already known about a process. In this respect, the researcher already knows the vicinity of the operating conditions in which an optimum point for a desired response variable resides. If this were not known, the researcher would start with what is known

as a screening experiment. This screening experiment was already performed at this point, and is the experiment referred to in section 2.2. For a more in depth explanation on this, in lieu of the following explanation, refer to the method of steepest ascent, which is elaborated on in section 11.2 of reference [21, p. 480].

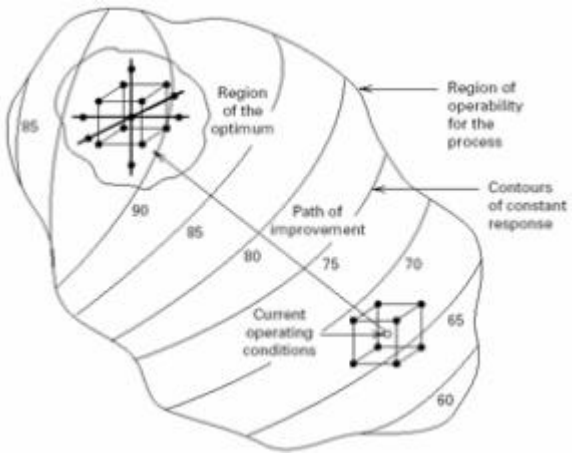

Figure 20: Pictorial Representation of Method of Steepest Ascent [21, p. 480]

Figure 20 is a good general example offered in Dr. Montgomery's book of how this method is useful. The cube on the bottom right labeled "Current Operating Conditions" represents the screening experiment that was performed in section 2.2. In this screening experiment, the factors were only varied between two levels in order to ascertain which of those factors affected the desired outcome, and how they affected it. If this "current operating region" already encompasses the region of the optimum for the desired response, as it does for this experiment, then the researcher employs an RSM experiment to find those settings which result in an optimum response. This is depicted by the cube with added center and axial points shown in the upper left of Figure 20. Had the screening experiment not encompassed the region of optimum response, the researcher would have performed one or more experiments with different ranges of those factors

that affect the outcome, such that the rate that the desirability of the outcome increased decreased, signaling a region with a local maximum.

Having performed these runs in the P5000, the next step is to characterize the samples using variable angle spectroscopic ellipsometry (VASE) for thickness, reflectivity, and absorptance, and to measure lifetime of the samples using Sinton Instruments WCT-120 lifetime tool. The VASE measurements are used to ensure that the a-SiN_x:H film is still optimal as an ARC. This section will only elaborate on the lifetime measurements, but these same VASE measurements are used for the experiment described in section 2.2. For silicon samples with lifetimes on the order of micro-seconds, such as are the cells made on the pilot line, a quasi-steady state photoconductance decay method (QSS) is used. This is achieved by illuminating the sample with a flash of light with a decay time much slower than the lifetime of the generated carriers. This situation approximates steady state generation in the sample. For more detailed information on the operating principles of Sinton Instrument's WCT-120 lifetime tool, the reader is referred to reference [24]. Those principles which are most pertinent to understanding the following experiment are explained here. Under steady conditions, the photoconductance of the sample is expressed as:

$$\sigma = qW\Delta n_{avg}(\mu_n + \mu_p) \qquad 4.2.1$$

In equation 4.2.1 W is the thickness of the sample, q is the elementary charge constant, Δn_{avg} is the average excess electrons/holes generated (assumed to be equal), and μ_n and μ_p are their mobilities. Much research has been done in the past regarding these mobilities in typical materials, such as silicon, and their dependence on injection level and sample doping are known. From the measured photoconductance σ, the

average excess minority carrier generation in these p-type base samples, Δn_{avg}, and their summed mobilities, ($\mu_n+\mu_p$), can be calculated. From these values, the effective generated carrier lifetime is calculated by:

$$\tau_{eff} = \frac{\sigma}{J_{ph}(\mu_n+\mu_p)} \qquad 4.2.2$$

In this equation, J_{ph} is the carrier generation rate, measured by a calibrated reference cell that is incorporated into the tool. A comparison to transient PCD measurements, also discussed in Dr. Sinton's paper, show that typical error for QSSPCD measurements on samples with lifetimes below 60μs are less than 1% [24].

Another key measurement used in these experiments is that of $J_{o,eff}$. This quantity is extracted from the inverse lifetime vs carrier generation curve, which as measured by the WCT-120 lifetime tool and its accompanying software is corrected for Auger recombination. This correction ensures that the curve produced is characteristic primarily of Shockley-Read-Hall (SRH) and surface recombination, which are the recombination mechanisms in which a solar cell process engineer is most interested. The $J_{o,eff}$ is calculated from the slope of a line fitted to the curve and is of the form:

$$J_{0,eff} = slope * (qWn_i^2) \qquad 4.2.3$$

This equation comes by way of Kane and Swanson's method for determining emitter saturation current density via contactless PCD [25]. For the samples used in this experiment, it can be shown that the contribution by bulk recombination to $J_{o,eff}$ is very small compared to the surfaces. This allows that a good approximation for $J_{o,F}$, the

contribution to $J_{o,eff}$ by recombination at the emitter/a-SiN_x:H film interface, can be made using the device structure depicted in Figure 21:

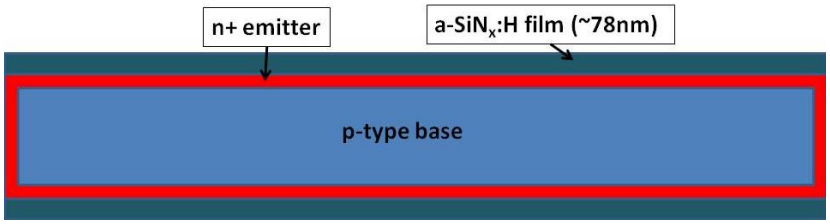

Figure 21: Double Side Sample Cross Section for $J_{o,f}$ Measurement

Assuming the principle of superposition holds for the measured $J_{o,eff}$, the contributions to it are the sum of $J_{o,F}$ and $J_{o,R}$, the front and rear interface components. Since the sample is symmetric, a reasonable estimation is then that these two are approximately equal. With these assumptions, the $J_{o,F}$ is estimated as half the measured $J_{o,eff}$. This measurement is the basis of the experiment discussed in section 4.3.

For the experiment discussed in this section, the effective lifetime of the samples are a sufficient response variable. These samples were made using round, 6 inch diameter, CZ grown, prime, 1-5 Ω-cm silicon wafers with a polished surface on one side. This type of substrate was used, because VASE is more accurate on a polished surface. However, the bulk lifetime of these substrates are comparable to those of the 156x156mm² pseudo square, mono-crystalline substrates that are used to make solar cells on the SPL pilot line.

4.2.3 a-SiN_x:H ARC Optimization Experiment: Results & Discussion

As was found in the experiment conducted in section 2.2, the optimum thickness and refractive index for an a-SiN_x:H ARC deposited by the P5000 at the SPL for the solar cells fabricated on the pilot line are 78nm and 2.0, respectively. Due to practical limitations of the P5000 PECVD tool, the temperature for this experiment is fixed at 350 ˚C. Using JMP to analyze the results, a response surface model that includes all squared terms and interactions, except the pressure squared term, was found to best correlate to the results. This model resulted in an R^2=0.99 for n as the response variable, and R^2=0.82 for $\ln(\tau_{eff})$ as the response variable. Using this model, JMP's prediction profiler estimates that for an a-SiN_x:H ARC with a thickness of ~78nm and a desired refractive index of n=2.03 at a photon wavelength of 630nm, the optimum parameter settings for the P5000 at the SPL are: pressure=3.4 Torr, RF power=300 W, and %SiH_4 in NH_3=49%.

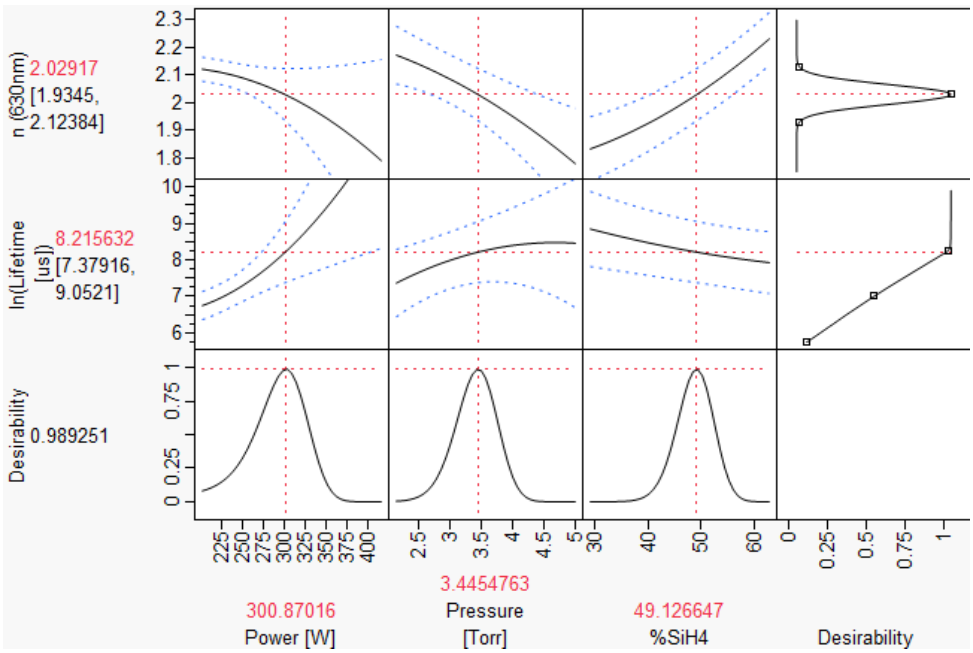

Figure 22: JMP Results for Optimum PECVD SiN_x ARC Deposition Parameters

As can be seen in the profiler, the error bounds (the blue dashed curves) of the predicted response for n are a little wide. These are set for a 95% confidence interval. In order to decrease this uncertainty, the design could have been replicated, but it is often the case in industry that replication is not practical. At the time of this experiment, replication was not practical. It has since been shown, however that this recipe for the SiN_x ARC does result in higher lifetime and higher J_{sc} samples.

A follow up experiment to this result was conducted in which 5 double sided emitter/ARC samples were processed in one lot, randomly distributed throughout a 13 sample lot, with the rest being full solar cells. The results of the full solar cells were spoiled by other processing problems at the time, and so will not be included here. Of the 5 double sided samples, two of the samples were deposited using the older, non-optimized recipe in the P5000 PECVD tool, and the other three were deposited using the

new optimized recipe. A t-test on the means of the lifetimes measured by QSSPCD method resulted in a mean difference of 8.7±0.6μs, with a p-value of 0.0007, meaning there is an estimated 0.07% chance of mistakenly concluding that the two recipes result in different lifetimes. Figure 23 shows another comparison on the mean lifetimes of these samples, in which a 95% confidence level is used to report the same result:

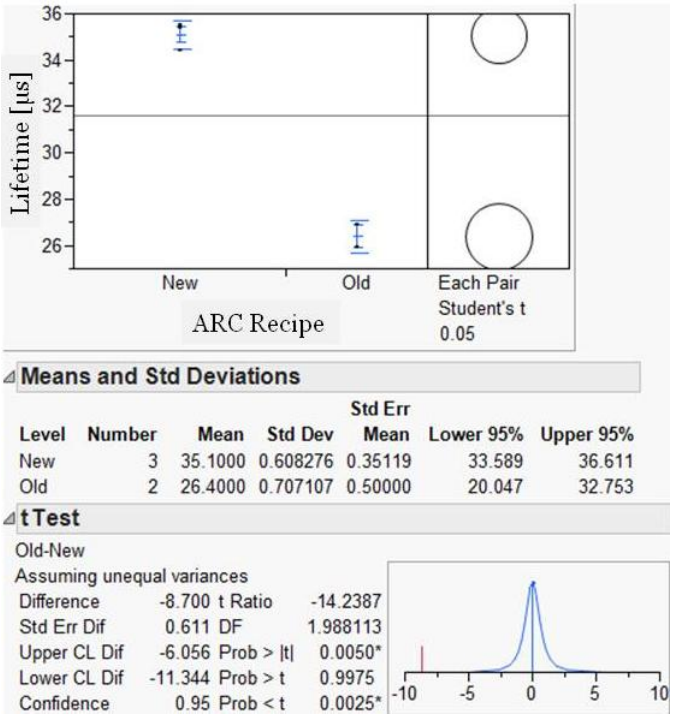

Means and Std Deviations

Level	Number	Mean	Std Dev	Std Err Mean	Lower 95%	Upper 95%
New	3	35.1000	0.608276	0.35119	33.589	36.611
Old	2	26.4000	0.707107	0.50000	20.047	32.753

t Test

Old-New
Assuming unequal variances

Difference	-8.700	t Ratio	-14.2387
Std Err Dif	0.611	DF	1.988113
Upper CL Dif	-6.056	Prob > |t|	0.0050*
Lower CL Dif	-11.344	Prob > t	0.9975
Confidence	0.95	Prob < t	0.0025*

Figure 23: Comparison of Mean Lifetimes for Two ARC Recipes

I would like to thank Bill Dauksher and Dr. Vivek Sharma for fabricating and characterizing these samples.

4.3.1 Passivating the Rear Surface

Passivating the rear surface of the cell, depending on the solar cell structure, can be a little less complicated than passivating the front surface. Though not the best quality of passivation achievable, a full coverage aluminum back contact offers several advantages over many competing technologies. The full-coverage aluminum back contact acts as a reflecting back layer, which increases photon absorption by the substrate. Upon inspection of the periodic table of elements, one can see that aluminum is a group III element, which acts as a p-type dopant in silicon. The reader can find a more detailed explanation of the physics that underlie the following discussion in many sources, but a reference that directly explains these phenomena in the context of solar cells can be found in the References section as [26].

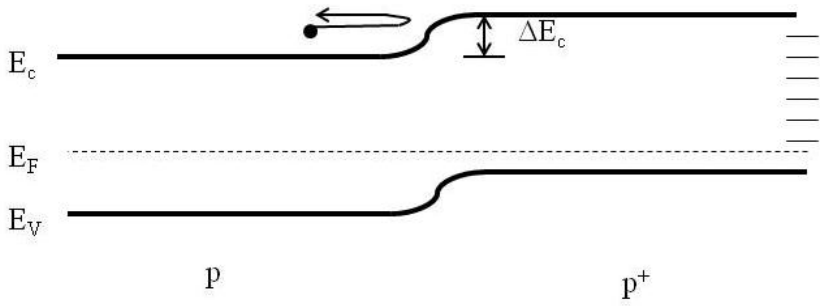

Figure 24: Band-Diagram Depicting Action of BSF

The benefit of the p^+-p junction formed at the back can be more easily visualized from the energy band-diagram of Figure 24. The higher doping of the back surface p^+ region results in an energy difference between the Fermi level and the valence band as compared to that of the moderately doped p region. In equilibrium, the Fermi levels must be flat and line up across the junction. This results in an energy step, or barrier, in the conduction band, denoted in Figure 24 as ΔE_C. As is shown, electrons with energies

less than ΔE_C will be reflected away from the rear surface, which is dense with surface recombination states. This has the effect of reducing the contribution of the rear surface to the dark saturation current J_o.

There are other BSF schemes which result in better passivation quality, but implementing them is not yet as simple as a printed and fired aluminum BSF. The following characterization and optimization are described in detail for this structure, but again, they are easily adapted to more advanced structures such as a diffused Boron BSF or passivated emitter and rear localized diffused BSF (PERL) cells.

4.3.2 $J_{o,BSF}$ Characterization & Optimization

In this experiment, the passivation quality of three printable aluminum metallization pastes were compared to each other by estimating their mean contributions to the reverse dark saturation current density, or $J_{o,BSF}$ of the cells made on the pilot line. These measurements were performed using Sinton Instruments' WCT-120 Photoconductance Lifetime Tester.

Using the same principle of assumed superposition described in section 4.2.2, the contribution to $J_{o,eff}$ by the rear surface, $J_{o,BSF}$, can be measured. The device structure used for this measurement is depicted in Figure 25:

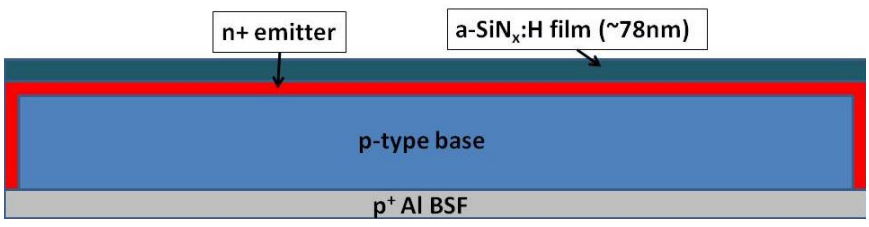

Figure 25: Cross Section of Device Used to Measure $J_{o,BSF}$

With proper correlation to the double sided emitter/a-SiN_x:H film samples, the estimated $J_{o,F}$ can be subtracted from the measured $J_{o,eff}$ of these samples to yield $J_{o,BSF}$.

In this equation, p_o refers to the equilibrium carrier concentration in the bulk of the wafer, and $n \approx \Delta n$ is approximately the carrier injection level.

4.3.3 BSF Paste Comparison: Setup & Procedure

The simplest means to compare metallization pastes to each other is to fabricate a number of solar cells utilizing the different pastes in a random order. This experiment is conducted here, but in parallel with another experiment in which the quality of surface passivation resultant for each paste is characterized. This is useful in two ways: 1) the results of this experiment will yield desired values used for modeling the solar cells made on the pilot line $J_{o,BSF}$, the component of reverse dark saturation current due to the BSF, and 2) it eliminates the uncertainty that is inherent in the IV measurements done on full solar cells. The test structures in this experiment have planar surfaces (not textured) and do not have a front silver contact grid. Thus, any uncertainty that would arise from areas of poor passivation of the front textured surface by a-SiN_x:H is greatly reduced for a planar surface, and any areas of poor contact of the emitter by the front silver contact grid is not an issue here.

Using principles of designed experiments, 3 pastes were randomly distributed across 27 samples, separated into 3 blocks. Three blocks were used, because at the time of the experiment, diffusing the emitter into the samples could only be done in runs consisting of at most 13 wafers. An additional 9 samples were included in the

experiment, 3 in each block, in order to extract $J_{o,front}$, which is the portion of the cell's dark saturation current due to the emitter/SiN_x ARC regions.

Due to the known non-uniformity of dopant density from sample to sample during diffusion, the double-sided emitter/SiN_x ARC samples were not randomized, but placed at the front, center, and rear of each block during diffusion. This would result in a fit of how $J_{o,front}$ varied with wafer position during diffusion. From the principles on which the lifetime tester operates, the $J_{o,front}$ is approximately half that of the $J_{o,eff}$ measured on these double-sided samples, since they are assumed to be symmetric. It is also assumed that the contribution of the bulk silicon to this effective dark saturation current is small compared to that of the surfaces. The samples were measured at an injection level of $5x10^{15}cm^{-3}$.

A model for the variation of the $J_{o,front}$ for the samples as a function of position during diffusion was then calculated. For each sample that was not a double-sided emitter/ARC sample, the estimated $J_{o,front}$ for that wafer position in that block is subtracted from the measured $J_{o,eff}$ for that sample to yield an estimate of the $J_{o,BSF}$. The experimental matrix used is shown in

Table 3: Experimental Matrix for Comparing BSF Pastes

Paste	Diffusion Slot #	Block #	Paste	Diffusion Slot #	Block #	Paste	Diffusion Slot #	Block #
Dbl-Sided	1	1	Dbl-Sided	1	2	Dbl-Sided	1	3
F5116	3	1	Franklin	3	2	Franklin	3	3
F5116	5	1	Franklin	5	2	F5116	5	3
F5132	7	1	F5116	7	2	F5132	7	3
Dbl-Sided	9	1	Dbl-Sided	9	2	Dbl-Sided	9	3
Franklin	11	1	F5116	11	2	F5116	11	3
F5116	13	1	F5132	13	2	F5132	13	3
F5132	15	1	F5132	15	2	F5132	15	3
Dbl-Sided	17	1	Dbl-Sided	17	2	Dbl-Sided	17	3
Franklin	19	1	Franklin	19	2	Franklin	19	3
F5132	21	1	F5132	21	2	Franklin	21	3
Franklin	23	1	F5116	23	2	F5116	23	3

The three pastes compared in this experiment are Ferro's 5116 and 5132 aluminum metallization pastes, denoted as F5116 and F5132 respectively, and Franklin's Lun-Al 988-F aluminum metallization paste, denoted as Franklin in

Table 3. The cells in this table which are labeled as "Dbl-Sided" under the "Paste" heading are not actually pastes, but are rather the double-sided emitter/ARC samples used to estimate the $J_{0,front}$ as a function of wafer position during diffusion.

Subsequent to diffusion, the resultant phosphosilicate glass (PSG) was removed in a 10:1 hydrofluoric acid (HF) in water solution. The sheet resistance of each sample was measured at approximately the center of the wafer on the side on which the emitter was formed, in order to confirm that the emitter was formed on each sample, and to profile how the dopant density varied with wafer position. Assuming a similar dopant density profile from wafer to wafer in each block, the R_{sh} is a good indicator of the total dopant present, and consequently a good indicator of how highly doped is the emitter near the surface. In theory, the measured R_{sh} is the inverse of the integration of the dopant density as a function of depth into the substrate [17].

In order to confirm the results of this $J_{0,BSF}$ experiment, another experiment was run in which full solar cells were fabricated using the 3 pastes. The run order for this experiment was not randomized, again due to the known non-uniformity of the emitter diffusion process at the time of these experiments. The positions of the cells during diffusion and their corresponding pastes are summarized in Table 4:

Table 4: Full Cell BSF Paste Compare Experimental Run Order

BSF Paste	Diffusion Position
F5116	1
F5132	3
Franklin	5

F5116	7
F5132	9
Franklin	11
F5116	13
F5132	15
Franklin	17
F5116	19
F5132	21
Franklin	23

The characterization of these samples include IV curve measurements using a Sinton Instruments FCT-250 flash tester and electroluminescence images (EL). The IV tester is common in industry. These type of measurements allow the fabricated cells to be sorted and matched based on their individual performance. For more information on the operation of the FCT-250, refer to reference [27]. In brief, the specific tester used at the lab flashes the sample with a pulse that varies from 0-1.9 Suns. During the initial pulse, the load is an open circuit, and the V_{oc} is measured every 56µs. This results in the calculation of the pseudo IV curve [28]. On the next pulse, the load is a short circuit, and the J_{sc} is measured. For the remaining light pulses, the load resistance is varied so that the current produced by the cell is measured at each load voltage from 0 to V_{oc}. From this curve, most of the pertinent characteristics of the cell are calculated, such as efficiency.

For more information on EL, see reference [29]. The electroluminescence tool utilizes a metal chuck and probing bars full of pogo pin probes, a DC power supply, and a charge-coupled device (CCD) camera. Carriers are injected into the cell in the dark using

the power supply and the probes. Although the majority of the carriers will recombine in a non-radiative fashion, there are a sufficient number of carriers that do recombine radiatively (i.e. band-to-band) to produce an infrared signal that can be detected by the CCD camera. A count of the number of photons detected for each CCD bin is recorded during the in which the shutter of the camera is open. The software used to resolve this information into an image bases the brightness of the resultant image on the difference between bins with the most and least counts. This is a useful technique for finding areas of solar cells where non-radiative recombination is large enough that radiative recombination is not detectable. These areas are dark in the resultant image. A good example of how defects are detected using EL can be seen in Figure 26:

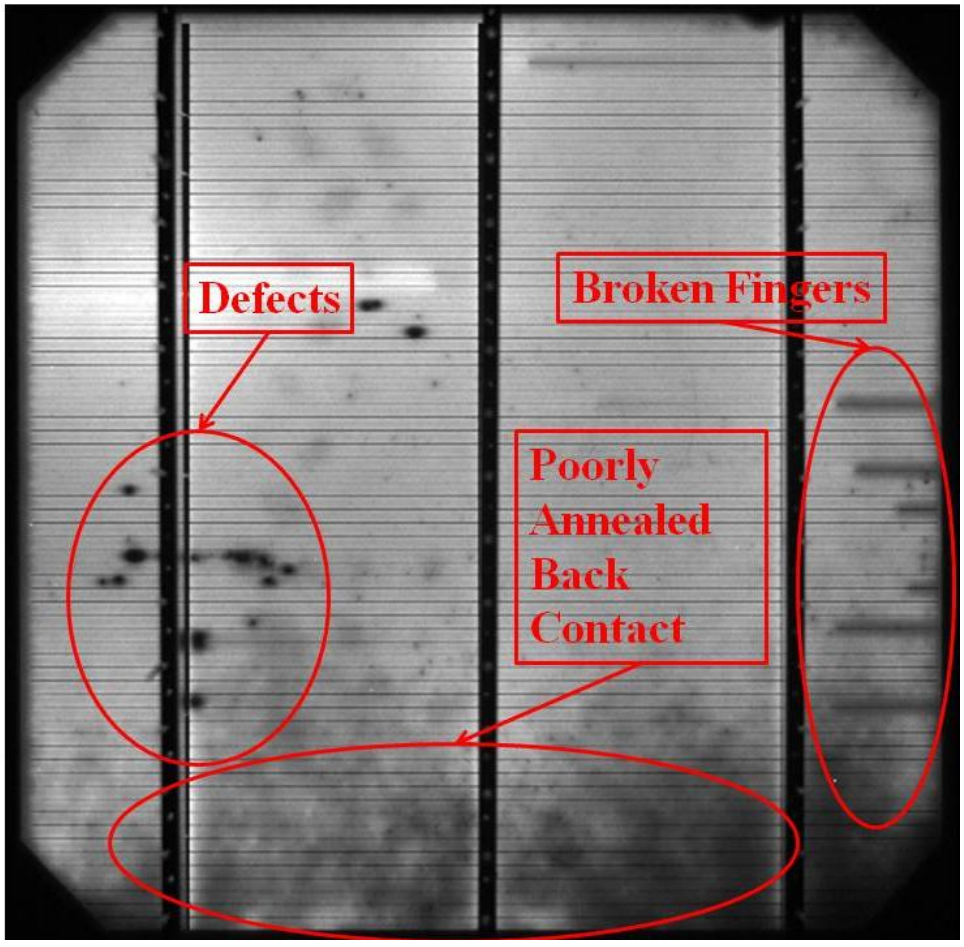

Figure 26: EL Image of a Poor SPL Solar Cell

This EL image is of a cell that was fabricated in 2012. The occurrence of all three of these defects has since been greatly reduced. EL was an essential tool for detecting them in the first place. The localized dark spots, labeled as "Defects" in Figure 26 are local shunts that were resulting due to the method used at the time to dry the back contact paste after printing. Eventually, the problem was narrowed down to the drying process, and a new, cleaner method was adopted to prevent this shunting in recent cells. The poorly annealed back contact was found to be due to insufficient control of the quartz IR lamps in the SierraTherm belt furnace used to fire cells at the SPL. A gamut of experiments was run, of which the cell in Figure 26 was a part, and as a result the firing process was optimized to where this non-uniformity across the back contact virtually no longer occurs. The broken fingers were found to be a result of insufficient print quality, due to many factors which cannot be quickly discussed in this section. One of the solutions to this recurring problem was to include a perimeter finger that connected all of the fingers to each other. This way, if one finger broke for any reason, some current can still flow through the adjacent fingers that are now connected to it by the perimeter finger. It is using these three methods that the results in the next section were obtained.

4.3.4 BSF Paste Comparison: Results & Analysis

After removing the PSG in BOE, the sheet resistance was measured at the center of each sample on the side on which the emitter was formed. This is to verify that the emitter was formed and is used as a measure of non-uniformity of dopant density across each block of the experiment. This non-uniformity also shows up in the $J_{o,eff}$

measurements. A plot which demonstrates the model fit for all 27 samples in this experiment is shown in Figure 27:

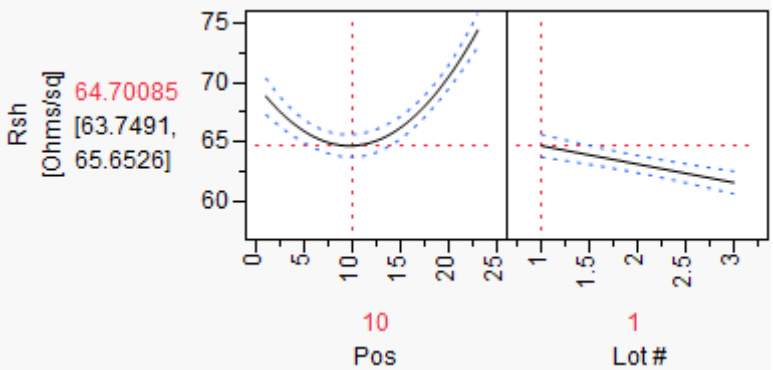

Figure 27: Prediction Profiler of R_{sh} vs Wafer Slot # and Block # with 5% Confidence Intervals Made Using JMP

The confidence intervals are calculated locally with wafer position and are proportional to the residual error in those regions. Although implementing this error in the actual model is difficult, it is useful to have when estimating the variation of $J_{o,front}$ vs. wafer position during diffusion in later analysis. The prediction model for this lot for R_{sh} as a function of wafer position during diffusion and block number is:

$$R_{sh} = 71.4156 - 1.0662x + 0.0549x^2 - 1.5445\beta$$

In this model, x is the sample's position during diffusion (i.e. its slot number), and β is the block number (i.e. 1, 2, or 3). Although this model will not be used in calculating the $J_{o,BSF}$, it is useful to have to confirm that the suspected trend of the non-uniformity resulting during diffusion correlates with the inverse trend that will be observed in $J_{o,eff}$.

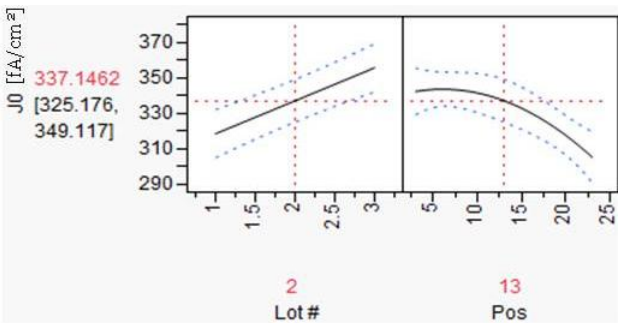

Figure 28: Prediction Profiler for the Model Used to Fit $J_{o,eff}$

From Figure 28, it can be seen that the effective dark saturation current follows a trend similar to the inverse of R_{sh} as a function of sample position during diffusion. This is expected, as it has been shown by other researchers in the past that $J_{o,eff}$ increases as the surface dopant concentration increases. For a more in depth explanation of this phenomenon, see reference [30]. The prediction equation used by JMP to create the profiles seen in Figure 28 is the following:

$$J_{o,eff}\ [fA/cm^2] = 306.8193 + 2.2484x - 0.1505x^2 + 18.5222(Lot\#)$$

In this and subsequent equations, x represents the sample's position during $POCl_3$ diffusion. Dropping the intercept term, 306.8193, the trend exhibited by $J_{o,eff}$ is then fitted to the calculated $J_{o,front}$ results for each of the double-sided emitter/ARC samples in each block. This is done by solving for β_o in the following equation for each double-sided emitter/ARC sample:

$$J_{o,e} = \beta_o + 2.2484x - 0.1505x^2 + 18.5222(Lot\#)$$

This results in the following three equations for each block:

Lot #1: $J_{o,front}= 132.3883+2.2484x-0.1505x^2$

Lot #2: $J_{o,front}= 139.8133+2.2484x-0.1505x^2$

Lot #3: $J_{o,front}= 142.3596+2.2484x-0.1505x^2$

Figure 29 is a plot for each of these equations which shows the estimated $J_{o,front}$ for each block as a function of wafer diffusion position:

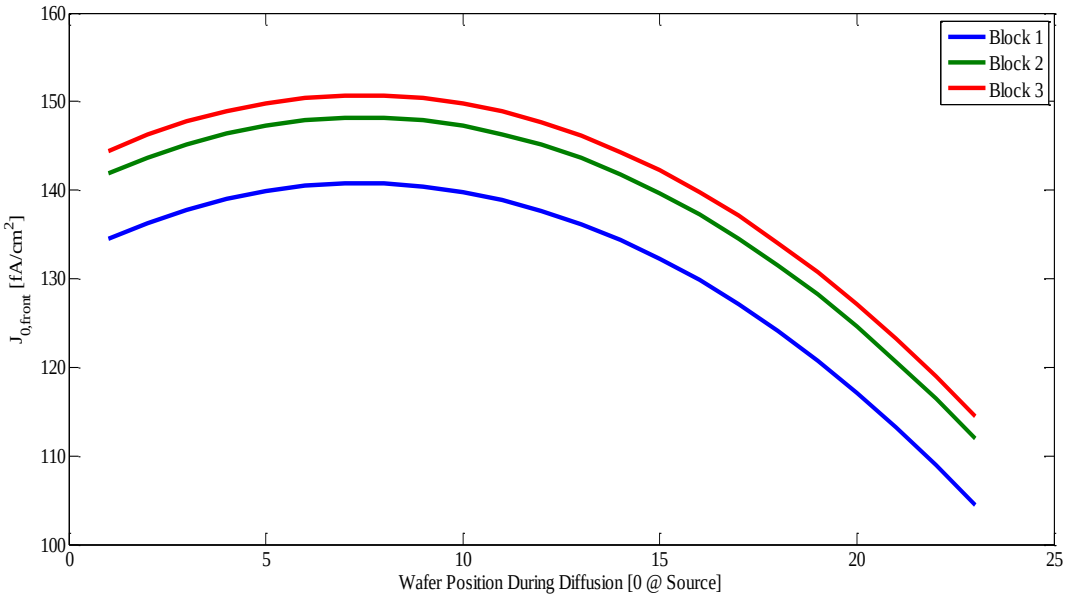

Figure 29: Modeled $J_{o,front}$ for the 3 Blocks

As was described in section 4.3.2, $J_{o,front}$ is then subtracted from each measured $J_{o,eff}$ to yield an estimate of $J_{o,BSF}$. The result of this analysis is presented in Figure 30:

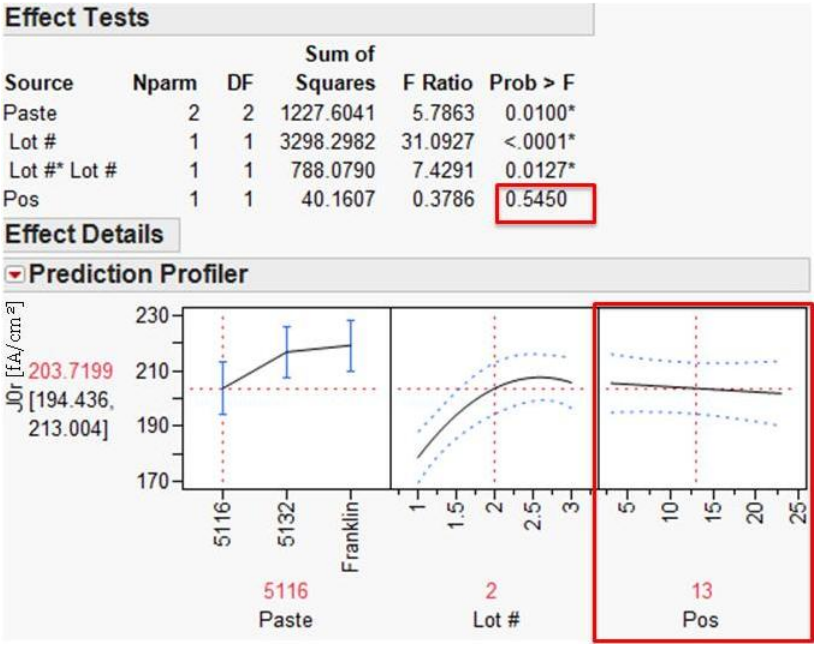

Figure 30: Effect of Sample Diffusion Position Removed from $J_{0,BSF}$

In Figure 30 the two red boxes highlight how the effect of wafer diffusion position has been effectively removed from the results, as intended. Figure 31 shows the results of a t-test comparing the three pastes to each other:

Least Squares Means Table

Level	Least Sq Mean	Std Error	Mean
5116	204.04782	4.3691484	196.407
5132	216.69778	4.3691484	209.057
Franklin	219.19840	4.3691484	211.558

LS Means Plot

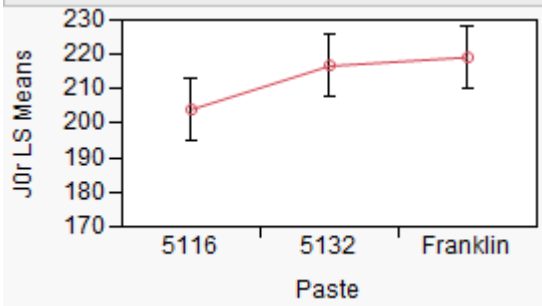

Level		Least Sq Mean
Franklin	A	219.19840
5132	A	216.69778
5116	B	204.04782

Levels not connected by same letter are significantly different.

Level	- Level	Difference	Std Err Dif	Lower CL	Upper CL	p-Value
Franklin	5116	15.15058	4.786162	5.22468	25.07647	0.0045*
5132	5116	12.64996	4.786162	2.72406	22.57585	0.0149*
Franklin	5132	2.50062	4.786162	-7.42527	12.42652	0.6066

Figure 31: Student's T-test Shows Ferro 5116 Paste Results in Lower $J_{o,BSF}$

From this final analysis, it is apparent that Ferro's 5116 aluminum metallization paste results in a lower $J_{o,eff}$ than the other two pastes for these cells. This is shown by the p-values for the difference between the means of Ferro's 5116 paste and the other two, 0.0045 and 0.0149. Thus one can conclude with 99.55% and 98.51% confidence that Ferro's 5116 paste outperforms Franklin's paste and Ferro's 5132 paste, respectively. These results are promising, but as was mentioned earlier, the interaction between the aluminum BSF pastes and the silver front contact paste being used should also be considered.

$$V_{oc,1} - V_{oc,2} = \frac{kT}{q}\left[\ln\left(\frac{J_{sc}}{J_{0,1}} + 1\right) - \ln\left(\frac{J_{sc}}{J_{0,2}} + 1\right)\right] \quad 4.3.4$$

Using this idealized relationship for the difference in V_{oc} between two cells, one with a Franklin BSF and the other with a Ferro 5116 BSF, an estimate of the gain in performance can be made. For a thermal voltage of 0.02585 V and a J_{sc} of 36mA/cm^2 for both cells, the estimated gain in V_{oc} for the Ferro 5116 sample is approximately 2mV. This very small potential gain is almost certainly trumped by other factors such as cost, yield, and compatibility with the front Ag paste while co-firing when deciding on which paste to use.

The results of the full cell experiment confirmed that the two Ferro pastes resulted in slightly better performance than the Franklin paste, but by a margin larger than predicted by the $J_{o,BSF}$ experiment. Cells utilizing Franklin's paste had a mean V_{oc} of 615mV. Ferro's 5132 aluminum paste resulted in a mean V_{oc} of 619mV, and the 5116 paste resulted in a mean V_{oc} of 620mV.

Means for Oneway Anova

Level	Number	Mean	Std Error	Lower 95%	Upper 95%
5116	4	0.620250	0.00141	0.61692	0.62358
5132	3	0.618667	0.00162	0.61483	0.62251
Franklin	3	0.615000	0.00162	0.61116	0.61884

Std Error uses a pooled estimate of error variance

Ordered Differences Report

Level	- Level	Difference	Std Err Dif	Lower CL	Upper CL	p-Value
5116	Franklin	0.0052500	0.0021490	0.000169	0.0103315	0.0446*
5132	Franklin	0.0036667	0.0022973	-0.001766	0.0090990	0.1545
5116	5132	0.0015833	0.0021490	-0.003498	0.0066648	0.4852

Figure 32: Results of JMP Analysis of BSF Paste Comparison Experiment

The conclusion that Ferro's 5116 outperforms Franklin's paste is made with 95.54% confidence. This is gleaned from the reported p-value by JMP of 0.0446. However, the same conclusion cannot be drawn with such confidence regarding the performance comparison between 5116 and 5132 or 5132 and Franklin. One of the reasons this seems somewhat illogical is that the results are heavily influenced by the too few number of samples for each paste. There were only 4 samples for 5116 and 3 samples each for 5132 and Franklin's paste. Franklin's paste, in particular, exhibits poor repeatability between samples as compared to the other two pastes. This behavior was observed in both the $J_{o,BSF}$ experiment and the full cell experiment.

This erratic behavior of the Franklin paste may be explained by the results of the EL imaging of the full cell samples. The electroluminescence images in Figure 33 show that the Franklin paste blisters during firing. These blisters are seen as dark spots all over the cell. Dark areas in an EL image usually correspond to non-radiative recombination or areas were no carriers are injected, as was explained in section 4.3.3.

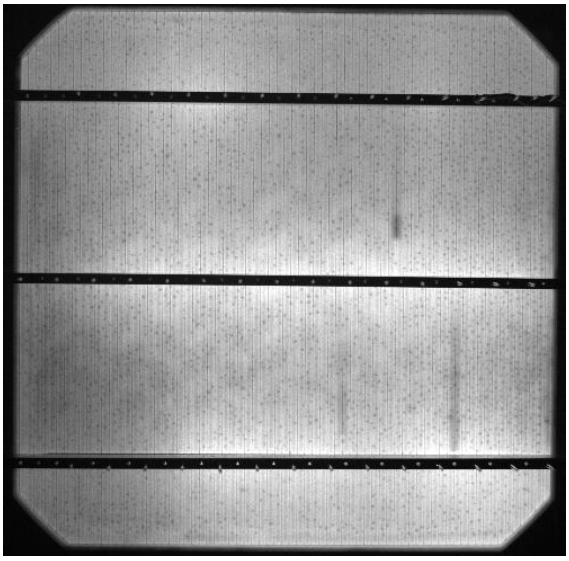

Figure 33: EL Image of Franklin Paste Cell

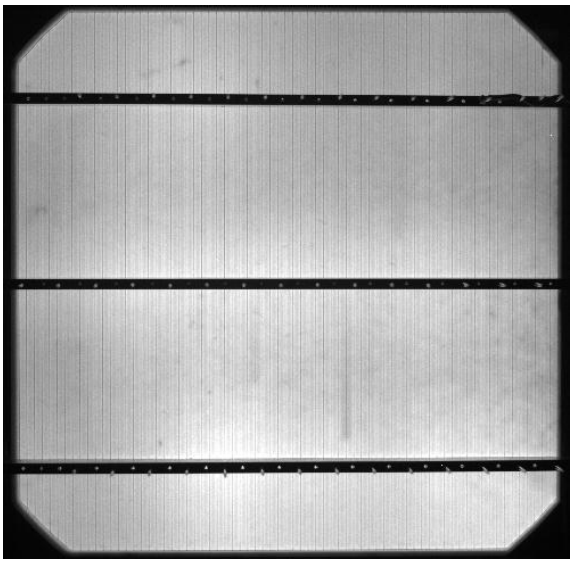

Figure 34: EL image of Ferro 5116 Paste Cell

4.4 Summary of Surface Passivation Quality Experimentation

As was mentioned in the introduction, the techniques used to characterize and optimize the surfaces of this specific solar cell structure are not exclusive of other solar cell structures. To make it easier for the reader to see the value in the presented experiments, the method and results will be summarized here.

Other than relying on full cell IV curve measurements, which may and will likely be affected by error due to other processes during cell fabrication, one can use the photoconductance decay (PCD) method to measure the quality of surfaces. The results of the PCD measurements will likely be dominated by areas of the sample with the highest recombination, usually one or both of the sample's surfaces. Therefore, if the researcher is interested in the properties of one surface, the other surface will have to be

passivated such that it results in a much lower contribution to J_o than the other. This also assumes that the bulk recombination, or recombination at other interfaces within the device are small compared to this surface. This is an important consideration when measuring multi-crystalline substrate devices, which is riddled with interfaces throughout its bulk.

If the other surface has a similar surface recombination rate as the surface of interest, than one can make a symmetric sample(s) in order to characterize this surface under the assumption that the measured $J_{o,eff}$ value is the superposition of the two surfaces. This is how the $J_{o,eff}$ of the front SiN ARC/emitter interface was estimated.

If it is suspected that the bulk properties of the sample, or the surface of interest is affected by one or more of the process steps for the corresponding full cell, then the principle of superposition can be used to formulate a scheme in which the properties of the surface of interest can be estimated. This was the case with the rear aluminum back-surface field. Here, the samples needed to undergo the diffusion process in order to be comparable with the full cells for which they are intended to characterize. This is because during the diffusion process, defects near the surfaces of the devices are either gettered out or deeper into the substrate where their effect on the full device performance is not as detrimental.

From the results of the PCD measurement, the researcher can ascertain the bulk lifetime and the reverse dark saturation current components, or the implied open-circuit voltage of cells that will be fabricated using the same processes. The results of these experiments can then be used to model the solar cells being studied to locate a specific area of interest within the device for troubleshooting or improvement.

For the front passivation experiments, the main outcome was an optimized a-SiN_x:H ARC deposition recipe. This recipe resulted in an optimum between the ARC's ability to passivate the surface and its ability to trap light. This was done by designing a response surface model experiment, which took into consideration the previously optimized thickness results that resulted in optimum light trapping capabilities. In this case, a thickness bounded around 77nm with an index of refraction bounded around n=2.00. Three parameters, pressure, RF power, and gas flow ratio SiH_4:NH_3 were varied, and the effective lifetime and index of refraction were the measured responses on which to optimize.

The main result of interest for the BSF characterization optimization experiments were that using QSSPCD method to measure the $J_{o,eff}$ was in good agreement with the results of a lot of full solar cells made using the same BSF pastes. Both experiments were run using principles of designed experiments such as blocking and randomization, which helped to resolve the error that is associated with both the measurements, and the variability in paste performance. The QSSPCD method also rids the comparison experiment of uncertainty associated with other processes incurred during the fabrication of full solar cells, and is therefore a reliable, effective alternative to characterizing the quality of a BSF. From this, it was ascertained that the Ferro 5116 aluminum paste results in a BSF quality similar to that of Ferro 5132, and outperforms the Franklin Lun-Al 988-F aluminum paste by an estimated 5mV in V_{oc}. The three pastes had effective surface recombination velocities ranging from 191 to 205 cm/s, a translatable difference of approximately 2mV, which isn't much, but can be used to model the cell structure's expected performance nonetheless.

5. Contact Formation

5.1 Contact Formation Principles: Emphasis on Screen Printing

There are many methods available for contact formation on photovoltaic devices. These include sputtering, buried contact, evaporation, roller printing, ink-jet printing, plating and others. They all exhibit their key advantages and disadvantages for different cell structures. For the cell structure that has thus far been discussed in detail in this work, screen printing is used. Screen printing of the metal contacts onto solar cells was first implemented in the 1970's, and has greatly streamlined and reduced the cost of manufacturing these photovoltaic devices. On a macroscopic level, the ratio of the area covered across the front surface of a solar cell by a silver grid to the area left exposed to light can be optimized using computer simulation. This is important because too much area coverage by silver reduces the amount of light that can be absorbed by the underlying silicon for electrical current generation. Too little silver coverage results in increased series resistance, since there will be fewer pathways for light-generated carriers to get extracted from the device. However, in the actual printing process, there are several factors that affect the performance of the device on a microscopic scale.

Figure 35: Silver Grid Contact Design for SPL Cells

Since series resistance is inversely proportional to the cross sectional area of the conducting finger (the grid line), it is desirable to have as large a cross sectional area as possible without drastically increasing shading of the cell. One way to do this is to increase the height of the finger and decrease the width. The ratio of the height to the width of a finger is known as the aspect ratio (AR), and it is best to maximize this ratio in order to decrease R_s. The aspect ratio can be better understood by observing Figure 36:

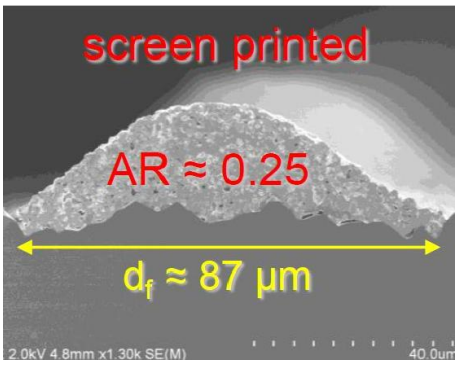

Figure 36: Cross-Sectional View of a Silver Finger on Silicon Taken by Scanning Electron Microscope (SEM)

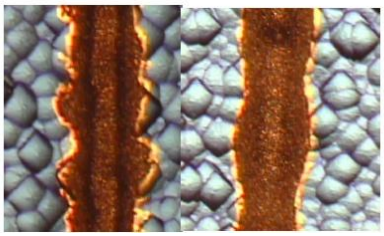

Figure 37: Microscope Image of Two Gridlines

In Figure 37, the gridline on the right has slumped more so than the gridline on the left. This results in a lower aspect ratio. Newer pastes typically have a higher viscosity, between 300-400 Pa·s, in order to prevent this slumping. This higher viscosity unfortunately makes high print quality much harder to achieve. Also, because of the already high viscosity upon receiving these pastes, it is very difficult to use a paste sample a second time after having opened it, as the solvents quickly evaporate out. This may prove difficult in an R&D environment, where ordering a new paste sample for each print session can be quite expensive, so it may be beneficial to use a Ag paste with a lower viscosity.

When printing, there are several factors that affect the aspect ratio, and subsequently the series resistance (R_s). However, R_s is affected by other aspects of the solar cell that may not be constant for every sample. This parameter can be affected by the doping profile that results for each cell during diffusion. It can be affected by the thickness and/or uniformity of the screen-printed back contact, and can also vary during the annealing stage wherein the printed metal contacts are fired in a belt furnace, but should problems arise during the experiment, the aspect ratio can be used as the response variable instead of R_s. The AR is only affected by printing parameters. It can be

measured optically using a calibrated microscope. By measuring the AR at 9 different points across the front contact of each sample, a mean AR and its uniformity can be estimated across each sample.

These processes are generally well controlled, and the error due to them should be taken care of through blocking, or by including their effects in the final analysis, as was done in the experiment in section 4.3. When printing, there are several factors that affect the aspect ratio, and subsequently the series resistance (R_s). However, due to limitations on varying some of these factors, as well as limitations on time and cost, only three factors are varied in the experiment described in this section. These factors are much cheaper in terms of time and cost to vary than other parameters such as contact design and screen parameters. Also, because the printing process is well understood at this point in the line's development, the experimental design to be implemented is a central composite design, which as was explained in section 4.2 is a response surface model (RSM).

The factors considered in the experiment are:

- Squeegee Pressure (P): This is actually the force on the squeegee in lbs.
- Squeegee Speed (SS): This is the speed at which the squeegee pushes the paste across the screen in in/s.
- Snap off Distance (SO): This is the distance between the screen and the solar cell in mils (thousandth of an inch)

All three factors have been found to interact in previous screening experiments with other pastes, and the same result is expected from this experiment. This makes sense from a physical standpoint, because the pressure and speed of the squeegee induce a shear force on the paste as it moves along the length of the screen. This shear force

temporarily reduces the viscosity of the paste, allowing it to flow through the stainless steel mesh and onto the solar cell's surface.

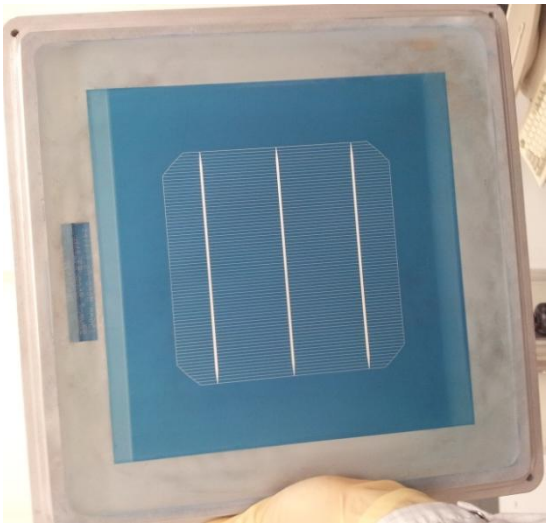

Figure 38: Screen Used for Front Contact Metallization

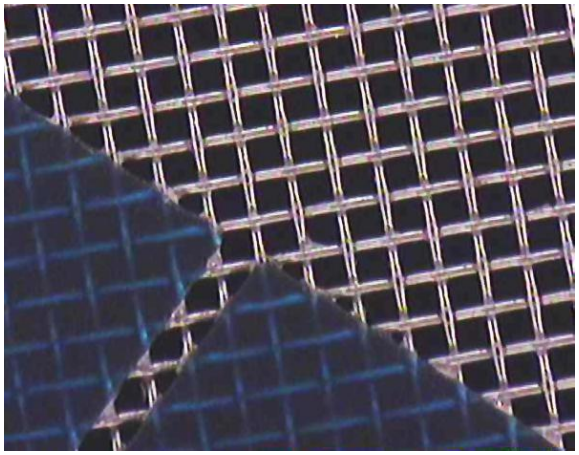

Figure 39: Close-up of Mesh and Emulsion of Screen

Figure 38 & Figure 39 show the screen used for this experiment and a close up of the stainless steel mesh and emulsion (blue). The snap-off distance dictates the angle

that is formed between the screen and the solar cell as the squeegee moves along the length of the screen. It is therefore expected that the larger the snap-off distance is, the more quickly the screen rises or snaps-off of the substrate, hence the name “snap-off distance”. The ranges of these three factors were chosen from experience, but are still rather large due to the lack of knowledge of this paste in particular, which is specified by the manufacturer to be half the viscosity of the paste previously used.

5.2 Contact Print Optimization: Experiment Design

The printer used to deposit the metal paste is an AMI MSP-9156PC semi-automatic screen printer. The screen was fabricated by Photo Stencil, and has a stainless steel mesh of density 290 threads crossing per square inch and a wire diameter of 0.8 mils. The paste for which this optimization experiment is intended is Heraeus SOL9610Y. At the time of this experiment, this paste was chosen because of its specified viscosity of 200 Pa·s, which was significantly lower and more manageable than the 350 Pa·s of the paste that was being used for the baseline cells. The three chosen factors to be varied are relatively cheap to change, as was discussed previously, however, making actual solar cells in order to measure current-voltage characteristics for each factor combination is not cheap.

Taking this into consideration, along with the results of screening experiments that had been run for other pastes in the past, it was decided that a face-centered central composite design, replicated once, with four center points would be sufficient to both reduce the inherent error associated with printing, and to keep the number of samples to

a reasonable number for an R&D pilot line. The reason a face-centered CCD was chosen is because either the high or low level factor for each of the parameters is a practical limit for the tool. Figure 40 shows this type of design. For those readers unfamiliar with this type of representation of a designed experiment, the 1's represent the high level of a factor and the -1's represent the low level of a factor.

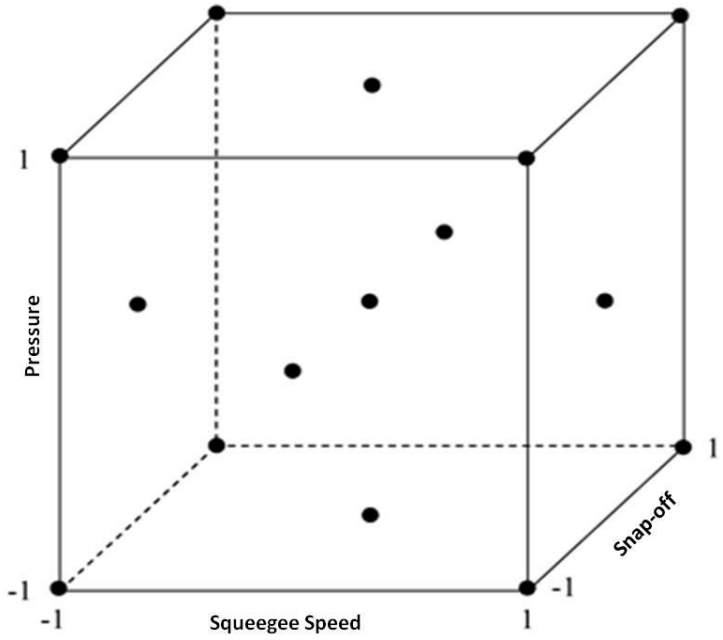

Figure 40: Face-centered Central Composite Design

The data will be blocked by the two lots (or replicates) of 21 wafers each. The cells in each lot are fabricated together, and so should have reasonably similar characteristics. Each lot contains the 16 cells of the un-replicated design, plus 5 extra cells whose purpose will be explained shortly. The un-replicated design for this experiment is outlined in Figure 41:

	tern	P [lbs]	SO [mils]	SS [in/s]
1	00A	21	80	12
2	000	21	80	7
3	A00	26	80	7
4	0a0	21	40	7
5	a00	15	80	7
6	+++	26	120	12
7	−+−	15	120	2
8	−++	15	120	12
9	00a	21	80	2
10	0A0	21	120	7
11	−−−	15	40	2
12	++−	26	120	2
13	−−+	15	40	12
14	+−+	26	40	12
15	+−−	26	40	2
16	000	21	80	7

Figure 41: RSM Design for Screen Print Optimization

The output response to be measured is the series resistance at the maximum power point. This series resistance is derived from the IV curve generated for each sample using the Sinton Instrument's FCT-250 tool described in section 4.3. The run order is randomized for each block in order to reduce error. In addition to these 32 cells that will be included in the experiment, there are 10 more cells that are fabricated for two reasons: 1) to replace any cells that break during fabrication, which is common as solar cells are inherently fragile, and 2) to test and vary the firing conditions prior to firing the remaining 32 cells. This is done because while the aluminum paste used to print the full-coverage back contact is sitting on a shelf in the solvent cabinet for a couple of weeks, the solvents in it slowly evaporate out, causing the paste's viscosity to increase. This usually results in a thicker back contact, which requires a higher temperature to anneal properly.

Thus the optimum firing recipe changes between solar cell lots. If not many of these extra cells are sacrificed, they will result in further replication.

5.3 Contact Print Optimization: Results & Discussion

After the experiment was run, 36 of the 42 cells could be analyzed. Of the 6 cells not included in the final analysis, 1 was fired with a different recipe than the other 41 cells, and 5 were broken at some point during processing. In the final analysis of the data set, there was a large variance that made modeling very difficult, which can be seen in the "lack of fit" shown in Figure 42:

Response Rs [mOhms]

Whole Model

Actual by Predicted Plot

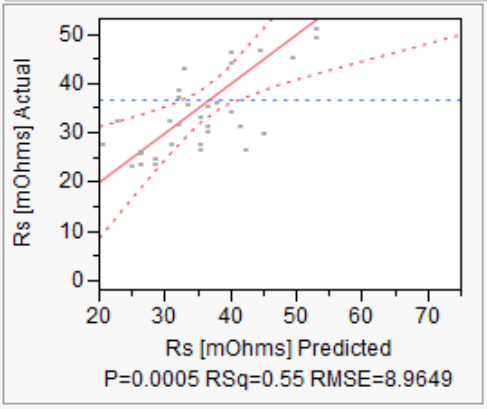

Summary of Fit

RSquare	0.545174
RSquare Adj	0.451072
Root Mean Square Error	8.964873
Mean of Response	36.72219
Observations (or Sum Wgts)	36

Analysis of Variance

Source	DF	Sum of Squares	Mean Square	F Ratio
Model	6	2793.6733	465.612	5.7934
Error	29	2330.6993	80.369	Prob > F
C. Total	35	5124.3726		0.0005*

Lack Of Fit

Source	DF	Sum of Squares	Mean Square	F Ratio
Lack Of Fit	22	2308.0267	104.910	32.3902
Pure Error	7	22.6726	3.239	Prob > F
Total Error	29	2330.6993		<.0001*
				Max RSq
				0.9956

Figure 42: Actual vs. Predicted Response Plot, Summary of Fit, ANOVA, and Lack of Fit for Final Model

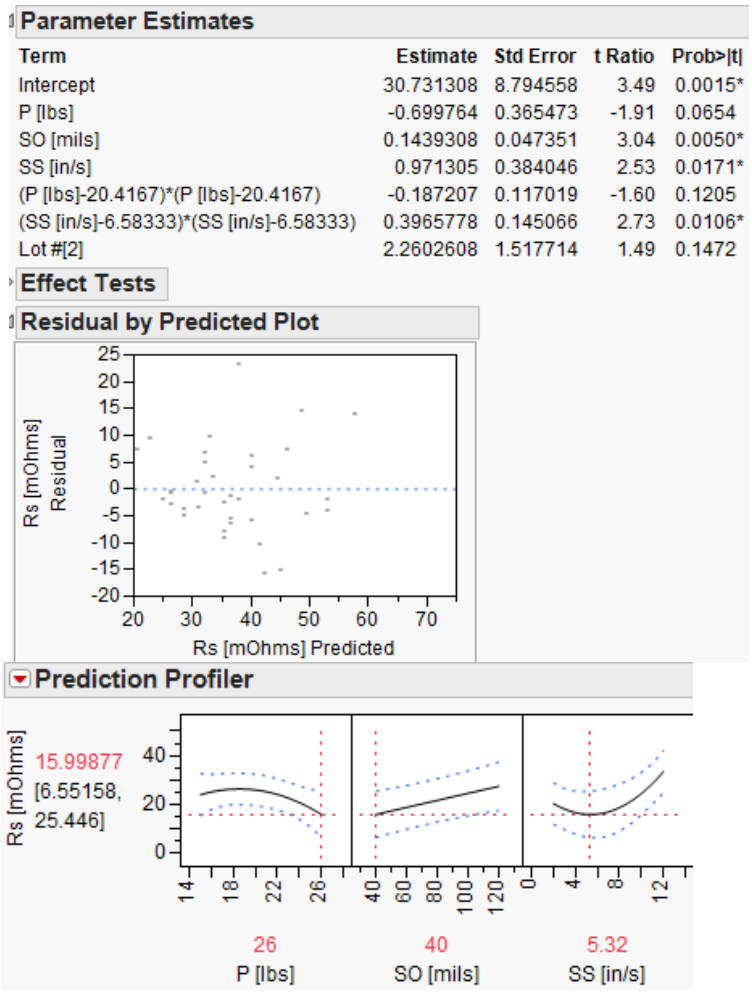

Figure 43: Parameter Estimates, Residual by Predicted Plot, and Prediction Profiler Set to Optimum Settings for the Final Model

This model predicts optimal settings of P=26 lbs, SO=40mils and SS=5in/s for this paste. As opposed to previous experiments run for other, more viscous pastes in the past, interaction terms were not important factors for this paste. It's important to note that for pressure, it would appear that a higher pressure might result in a lower R_s, but 26 lbs is approximately the maximum before the fragile silicon substrates begin to break on a regular basis. As for the snap-off distance, the method used to find the zero point

(i.e. where the screen is touching the substrate) is not very accurate. A snap-off setting less than 40 mils will likely result in the screen lying on top of the substrate throughout the entire print cycle. This would result in the majority of the paste that had been deposited, being lifted back off when the screen rose off the substrate after the squeegee completed its cycle. Thus 40 mils is the lowest practical setting.

Although this model has a relatively low R^2 value of 0.55, visual inspection of the samples reveal that these settings did produce the best prints. When observed from a low angle to the surface of the solar cell, the quality of these prints can be seen by eye, as is depicted in Figure 44, Figure 45, & Figure 46:

Figure 44: Great Print

Figure 45: Reasonable Print

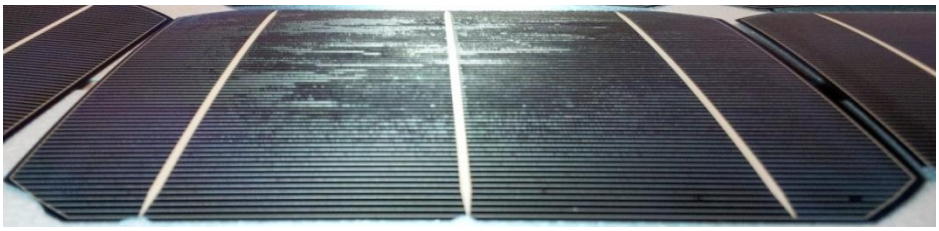

Figure 46: Horrible Print

All 36 cells were inspected this way, and a general trend was confirmed in which cells printed with a slower squeegee speed, a lower snap-off distance, and a higher pressure exhibited excellent prints when using Heraeus SOL9610Y Ag paste. The most probable cause of the large error that resulted in this experiment is the aluminum back contact printer. It had been experiencing problems during the time of this experiment, in which there had been air leakage in the squeegee pressure assembly. This yields poor control of the back contact thickness, and for a few of the samples resulted in the wafer sticking to the bottom of the screen, further compromising the uniformity of the back contact. The thickness and uniformity of the local thermal mass of the back contact is important to have uniform characteristics during the contact firing step. An unrelated lot of solar cells that was run 1 week after this experiment resulted in even higher series resistance.

Thirty-seven samples distributed across two lots was analyzed subsequent to this experiment. They were printed with this same paste sample, meaning it was from the same jar of paste, and these optimum printer settings.

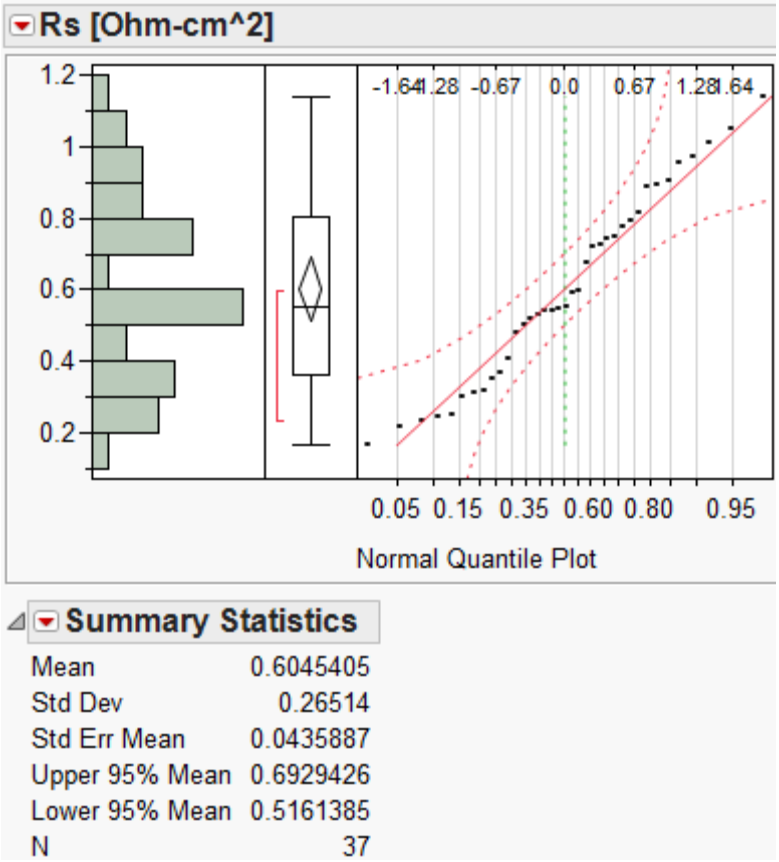

Figure 47: R_s Statistics of Solar Cells Printed Subsequent to Print Optimization

As can be seen in Figure 47, cells printed with these optimal printing settings repeatably exhibit series resistance at the maximum power point of 0.605±0.265 Ω-cm² for a 95% confidence interval, which is an excellent result. This result was reported for 37 samples. Therefore, despite a less than desirable R^2 value for the analysis of the results of this experiment, the outcome was still useful. This again demonstrates the utility in learning and implementing design of experiment principles in a pilot line setting. The characterization technique applied in this experiment is applicable to every contact formation scheme for any PV structure. To diagnose specific problems in contact formation, there are other more elaborate measurement techniques, such as transmission line measurement [17, p. 139], which will yield information about specific

contact resistance between the grid and the substrate. For a high throughput process that has already been developed, as has this one, series resistance via IV curve generation is the least expensive characterization method that directly correlates contact quality to final cell performance.

6. CONCLUSION

In this thesis, the utility of a micro-scale R&D pilot line was explicated, and the methods used for developing a pilot line were illustrated in detail. The hope is that this work will be used by future photovoltaic device engineers seeking to launch a PV pilot line, to do so with little nescience. An emphasis has been put on designed experiments to increase the efficiency with which experiments are conducted on a pilot line by increasing result resolution while decreasing the number of samples needed. Figure 48 shows how the pilot line was developed over the course of a year using these methods:

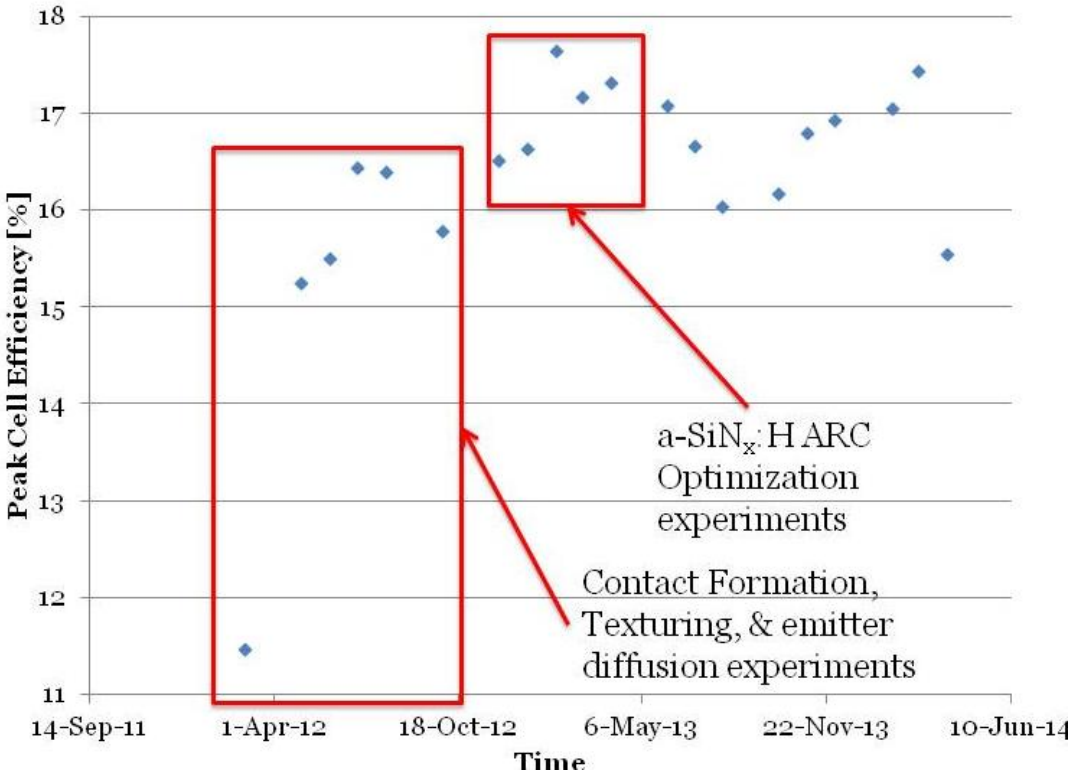

Figure 48: Plot of Cell Efficiency vs Time at SPL

Highlighted within the plot are two keys aspects of the student-led pilot line. One important aspect is that the students who are taught these experimental design techniques have a direct impact on the efficiency of the cells fabricated on the pilot line. The other highlight shows at what period in time in the development of the pilot line these techniques were implemented, which shows how their use affected the overall performance of the pilot line.

Many of the underlying physics principles that explain the phenomena described in the preceding work were glossed over in favor of focusing on the practical outcomes for the researcher's sake. However, references where these explanations and results could be found were included where appropriate. For more complex problems that are not included, but are alluded to at appropriate times, references are included with the same goal. Given the chronological manner in which these methods were presented, which follows the typical fabrication process, it is intended that this document serve as an easily digested guide for researchers developing a PV pilot line. This should expedite not only the development process, but also the troubleshooting of problems encountered on the line, as many of the problems encountered during the development of this line are described along with their solutions.

REFERENCES

[1] P. Speser, "The Art and Science of Technology Transfer," Hoboken, New Jersey, Wiley & Sons, 2006.

[2] A. Evans, V. Strezov and T. Evans, "Comparing the Sustainability Parameters of Renewable, Nuclear and Fossil Fuel Electricity Generation Technologies," 2010. [Online]. Available: www.worldenergy.org/documents/congresspapers. [Accessed 14 January 2014].

[3] US Department of Energy, "Crystalline Silicon Photovoltaics Research," 20 November 2013. [Online]. Available: http://www1.eere.energy.gov/solar/sunshot/pv_crystalline_silicon.html. [Accessed 20 December 2013].

[4] Encyclopaedia Britannica, "Silicon-Si," 2013. [Online]. Available: http://www.britannica.com/EBchecked/topic/544301/silicon-Si. [Accessed 20 December 2013].

[5] S. Lacey, "Top Chinese Manufacturers Will Produce Solar Panels for 42 Cents per Watt in 2015," Green Tech Media, 4 February 2013. [Online]. Available: www.greentechmedia.com. [Accessed 14 January 2014].

[6] ISFH, "19.6% Efficient Large Area Fully Screen Printed Silicon Solar Cells," ISFH, [Online]. Available: http://www.isfh.de/institut_solarforschung/industrienahe-siebdrucksolarzelle.php?_l=1. [Accessed 6 February 2014].

[7] Spire Solar, "Fully Automated High Efficiency Cell Lines," Spire Solar, 2011. [Online]. Available: http://www.spirecorp.com/spire-solar/solar-cell-and-wafer-lines/index.php. [Accessed 6 February 2014].

[8] M. Blech, A. Laades, C. Ronning, B. Schroter, C. Borschel, D. Rzesanke and A. Lawerenz, "DETAILED STUDY OF PECVD SILICON NITRIDE AND CORRELATION OF VARIOUS," [Online]. Available: http://www.cismst.org/fileadmin/user_upload/news/Blech_1CV.4.30_Preprint_24_EPVSEC_Hamburg.pdf. [Accessed 9 February 2014].

[9] R. Nave, "Hyperphysics Anti-reflection coatings," Georgia State University, 2013. [Online]. Available: http://hyperphysics.phy-astr.gsu.edu/hbase/phyopt/antiref.html. [Accessed 9 February 2014].

[10] C. Honsberg and S. Bowden, "PVCDROM," [Online]. Available: http://www.pveducation.org/pvcdrom/properties-of-sunlight/atmospheric-effects.

[Accessed 9 February 2014].

[11] S. Bowden and C. Honsberg, "Spectral Response," Solar Power Lab, 2012. [Online]. Available: http://pveducation.org/pvcdrom/solar-cell-operation/spectral-response. [Accessed 24 March 2014].

[12] National Renewable Energy Laboratory, "Reference Solar Spectral Irradiance," December 2013. [Online]. Available: http://rredc.nrel.gov/solar/spectra/am1.5/. [Accessed 21 March 2014].

[13] S. Herasimenka, *Process PhD Comprehensive Exam: Development for 20% Silicon Heterojunction Solar (SHJ) Cell and Analysis of Loss Mechanisms,* Tempe, 2013.

[14] E. Vazsonyi, K. De Clercq, R. Einhaus, E. Van Kerschaver, K. Said, J. Poortmans, J. Szlufcik and J. Nijs, "Improved anisotropic etching process for industrial texturing of silicon solar cells," *Solar Energy Materials & Solar Cells,* vol. 57, pp. 179-188, 1999.

[15] D. Kumar, S. Saravanan and P. Suratkar, "Effect of Oxygen Ambient During Phosphorous Diffusion on Silicon Solar Cell," *Journal of Renewable and Sustainable Energy,* no. 4, p. 033105, 2012.

[16] R. Ronen and P. Robinson, "Hydrogen Chloride and Chlorine Gettering: An Effective Technique for Improving Performance of Silicon Devices," *Journal of the Electrochemical Society ,* vol. 119, no. 6, pp. 747-752, 1972.

[17] D. Schroder, Semiconductor Material & Device Characterization, Hoboken, New Jersey: John Wiley & Sons, 2006, p. 9.

[18] K. Taniguchi, K. Kurosawa and M. Kashiwagi, "Oxidation Enhanced Diffusion of Boron and Phosphorus in (100) Silicon," *Journal of the Electrochemical Society,* vol. 127, no. 10, pp. 2243-2248, 1980.

[19] V. Prajapati, J. Horzel, P. Choulat, T. Janssens, J. Poortmans and R. Mertens, "Oxidation Enhanced Diffusion on p-type PERC silicon Solar Cells," in *EU PVSEC*, Frankfurt, 2012.

[20] N. Cheung, "EE143 Lecture 10," 16 February 2006. [Online]. Available: http://www-inst.eecs.berkeley.edu/~ee143/sp06/lectures/Lec_10.pdf. [Accessed 26 March 2014].

[21] D. Montgomery, Design and Analysis of Experiments, Hoboken: John Wiley & Sons, 2013, p. 480.

[22] A. Aberle, "Overview on SiN Surface Passivation of Crystalline Silicon Solar Cells," *Solar Energy Materials and Solar Cells,* vol. 65, no. 1-4, pp. 239-248, 2001.

[23] V. Sharma, "ASU Repository," August 2013. [Online]. [Accessed 18 March 2014].

[24] R. Sinton, "Contactless determination of current–voltage characteristics and minority-carrier lifetimes in semiconductors from quasi-steady-state photoconductance data," *Applied Physics Letters,* vol. 69, no. 17, 1996.

[25] D. E. Kane and R. M. Swanson, "Measurement of the Emitter Saturation Current Density by a Contactless Photoconductivity Decay Method," in *18th IEEE PVSC* , Las Vegas, 1985.

[26] J. Nelson, "7.4.5 Strategies to Reduce Surface Recombination," in *The Physics of Solar Cells*, Covent Garden, Imperial College Press, 2004, pp. 191-193.

[27] Sinton Instruments, "Sinton Instruments," [Online]. Available: http://www.sintoninstruments.com/PDFs/Sinton-FCT-CCT-Cell-Tester-product-note.pdf. [Accessed 15 3 2014].

[28] S. Bowden and C. Hansberg, "Jsc-Voc and Suns-Voc," [Online]. Available: http://www.pveducation.org/pvcdrom/characterisation/jsc-voc-and-suns-voc. [Accessed 15 March 2014].

[29] S. Bowden and C. Honsberg, "Electroluminescence," [Online]. Available: http://www.pveducation.org/pvcdrom/characterisation/electroluminescence. [Accessed 15 March 2014].

[30] R. R. King, R. A. Sinton and R. M. Swanson, "Studies of Diffused Phosphorus Emitters: Saturation," *IEEE Transactions on Electron Devices,* vol. 37, no. 2, pp. 365-371, 1990.

[31] Alcatel Lucent, "Bell Labs Celebrates 50th Anniversary of the Solar Cell," 26 April 2004. [Online]. Available: www3.alcatel-lucent.com. [Accessed 14 January 2014].

[32] W. E. Jellett and K. J. Weber, "Accurate Measurement of Extremely Low Surface Recombination Velocities on Charged, Oxidized Silicon Surfaces Using a Simple Metal-Oxide-Semiconductor Structure," *Applied Physics Letters,* pp. 90-92, 2007.